UNIVERSITÀ DEGLI STUDI DI PADOVA

Dipartimento di Fisica e Astronomia "Galileo Galilei"

Master Degree in Physics

Final Dissertation

Commissioning Experiment of the

AGATA+MUGAST+VAMOS Setup for Direct Reaction

Studies

Thesis Supervisor

Prof. Daniele Mengoni

Thesis Co-supervisor

Marlène Assié

Candidate

Andrea Raggio

Academic Year 2019/2020

Abstract

In this work, the commissioning experiment performed at GANIL of a new cutting-edge detection setup for the study of direct reactions is described. The setup consists in the state of the art gamma-ray tracking array AGATA, the charged particle array MUGAST to define the reaction kinematics, and the magnetic spectrometer VAMOS for discrimination of the heavy-ion products.

The neutron transfer reaction $^{16}O(d,p)^{17}O$ was chosen as a reference because it was performed in the past both in direct and inverse kinematics and at different energies. The coincident measurement of the outgoing proton and gamma-ray from the $1/2^+$ first excited state in ^{17}O allowed the characterization of the setup and its tuning for the subsequent physics campaign.

The angular distributions of the transfer reaction to the $5/2^+$ (g.s.) and $1/2^+$ ^{17}O levels were measured and compared to theoretical DWBA calculations. Finally the efficiency of AGATA during the experiment was computed and compared with expectation.

Contents

1 Introduction

Direct observation of phenomena drove physics and science in general for years, however with the advancements in knowledge and the discovery of the microscopic world of the atom this was no longer possible. New techniques were needed to exploit these otherwise unreachable information.

At the beginning of the 20th century, Ernest Rutherford, one of the father of nuclear physics, leaded an experiment where a beam of alpha particles impinged on a thin gold target. The observation of the outgoing products from the collision gave precise information on the atomic structure, allowing the physicist to derive the so called Rutherford atomic model.

The technique of colliding different particles or nuclei is nowadays one of the main investigation tool to understand the microscopic world, both in high and low energy physics. In the latter, the advent of radioactive ion beam facilities grants the possibility to probe the structure of unstable nuclei far from the valley of beta stability.

The interaction between the constituents of the beam and the target could happen through a set of different reactions (see Fig. 1.1), which are classified in two main families:

Direct reaction, involving peripheral collisions, such as elastic/inelastic scattering and transfer processes.

Compound nucleus reaction, where a fusion between the two input nuclei occurs, such as fusion evaporation processes.

This work will focus on the first one, by the description of an experimental setup, AGATA-MUGAST-VAMOS, designed specifically to study direct reactions, coupling a set of three different detection systems. The commissioning experiment of this apparatus, held at GANIL laboratories the first week of April 2019, will be reported.

This work is divided in four different chapters. Initially, the reaction chosen for this experiment is presented and motivated.

Second chapter presents a theoretical description of the scattering problem, with emphasis on the reproduction of the differential cross section of the involved processes.

Third chapter presents a detailed description of the three detection systems which compose the setup.

The analysis of the acquired data from this commissioning is described and discussed in the fourth and final chapter.
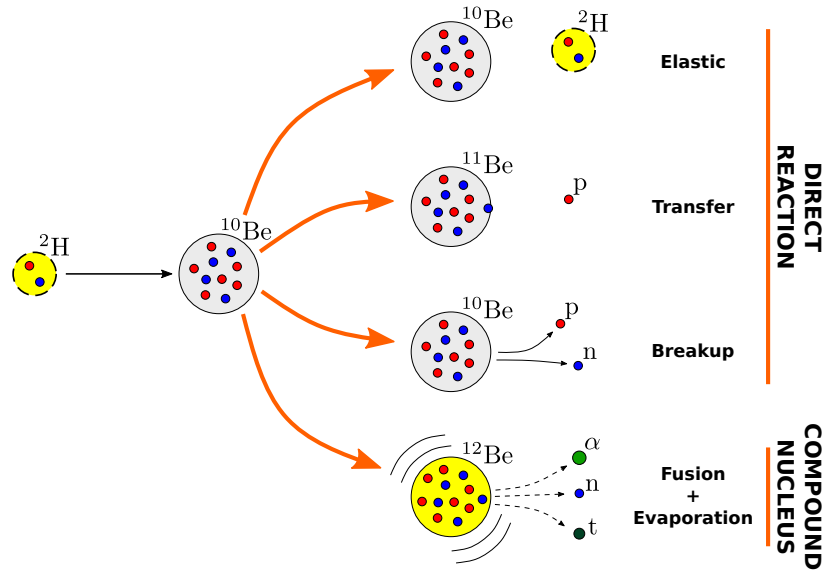

Figure 1.1: Example of direct and compound nucleus reaction channels taking place in a d + ^{10}Be collision.

1.1 Commissioning Reaction

A commissioning experiment, prior to the experimental campaign, is a crucial step to validate the correct coupling between the different systems of the AGATA-MUGAST-VAMOS setup, used here for the first time. The possibility to find in advance and correct eventual issues is the main purpose of the commissioning, in this sense a total of 8 UT (1 UT = 8 h.) were scheduled starting from 04.04.2019 .

The reaction chosen for this experiment is a neutron transfer process performed in inverse kinematic. A beam of ^{16}O with an energy of 6 MeV/u was sent to a deuterated polypropilene CD2 target. The channel of interest is the interaction of beam nuclei with target deuterium, producing a proton and ^{17}O, the net result is therefore the transfer of a neutron from deuterium to ^{16}O initial nuclei. This particular process was chosen because extensively studied in the past [1, 2, 3, 4] at different energies and both in direct/inverse kinematics. As reference the differential cross sections measured by M. D. Cooper et al. in [1] is reported in Fig. 1.2.
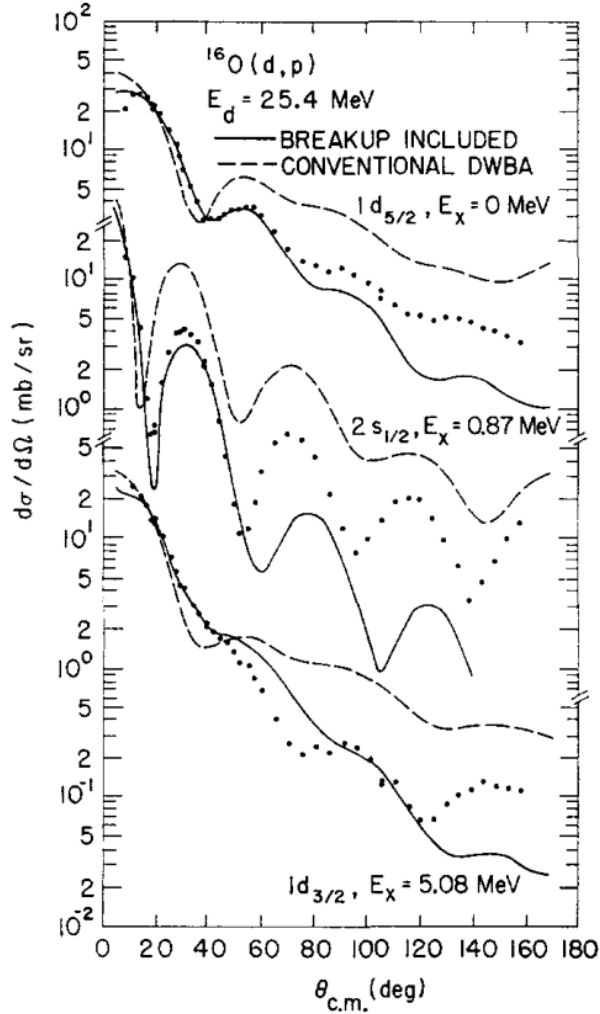
Figure 1.2: Measured differential cross sections for the direct kinematic transfer $^{16}O(d,p)^{17}O$ measured by M. D. Cooper et al. in [1]. The experimental points are compared to the DWBA theoretical distributions.

Beam energy was chosen to optimize the matching and cross section to the state of interest in ^{17}O. A lower value would not have been possible because the proton would have been emitted with too low energy. The process is quite favorable in terms of statistics because the Spectroscopic Factor between the ground state of ^{16}O and the first excited state of ^{17}O is close to unity. All this characteristics make this reaction a good reference for a benchmark test.

The experiment populates via one-neutron stripping reaction the g.s. $(5/2^+)$ and first excited state $(1/2^+)$ of ^{17}O (see Fig. 1.3) involving a transfer of $l = 2$ and $l = 0$ angular momentum, respectively. The $1/2^+$ excited state decay through an E2 gamma-ray emission of 870.71 keV with a characteristic lifetime of 179.2 ps.
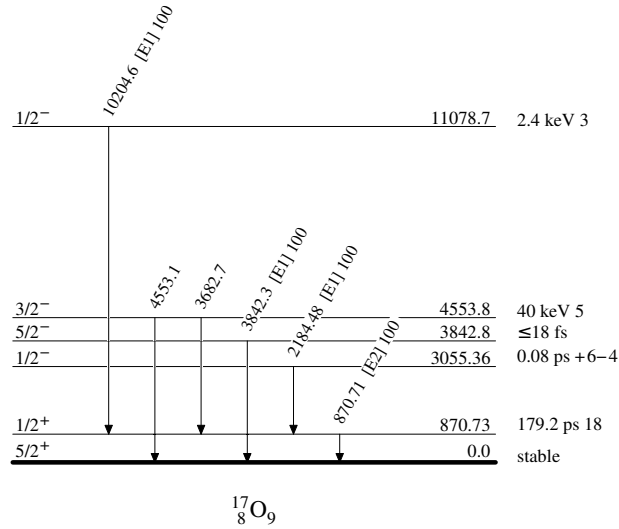
Figure 1.3: Level scheme of ^{17}O.

The kinematic proprieties of the reaction are reported in Fig. 1.4. The heavy residual nucleus is emitted in the laboratory frame at forward angles within a cone of $\sim 5.4°$, while the proton ejectile covers the whole solid angle. Nevertheless proton emission is mainly backward due to the strongly peaked differential cross section at low center of mass angles.
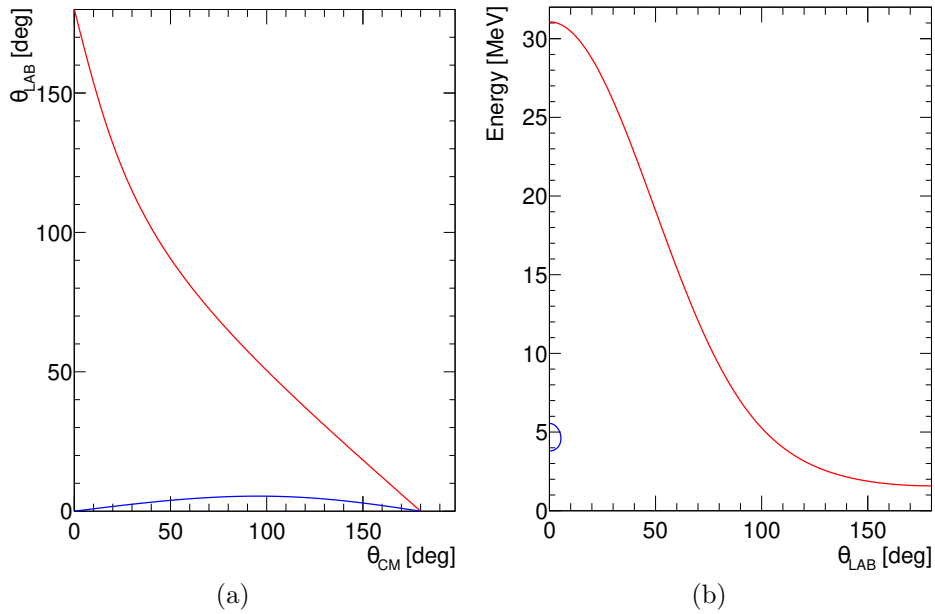

(a)   (b)

Figure 1.4: Laboratory angle as a function of center of mass angle for proton (red) and ^{17}O (blue) (a) and their kinematic lines (b).

4

2 Scattering Theory

A nuclear collision is in general a complicated many-body quantum-mechanical scattering problem, without a precise solution in the majority of the cases. The only way to solve this problem is the use of approximated models tailored to specific kind of reaction, limiting the degree of freedom activated by the interaction.

In order to compare measured data with theoretical models a quantity independent from the experimental conditions is needed. For this reason the concept of Cross Section is defined. Considering a beam of profile S impinging on a target of thickness ΔX, the number of beam particles after the target will be $N' = N - \Delta N$, where ΔN is the number of particles lost by the beam due to target interaction. Defining σ the geometrical area within the nuclear collision occurs and n_X the number of scattering centers per unit volume of the target, the following expression is obtained:

$$\frac{\Delta N}{N} = \frac{n_X \left(S\Delta X\right)\sigma}{S} = n_X \Delta X \sigma \tag{2.1}$$

In terms of reaction rate and beam intensity:

$$\frac{R_{reaction}}{I_{beam}} = n_X \Delta X \sigma \tag{2.2}$$

Dimensionally the cross section σ is an area multiplied by the probability that the reaction can occurs. It is useful to define also the differential cross section:

$$\frac{d\sigma}{d\Omega}(\theta, \phi) = \frac{r(\theta, \phi)}{4\pi I_{beam} n_X \Delta X} \tag{2.3}$$

$r(\theta, \phi)$ is the normalized angular distribution of the reaction products. The relation between σ and the differential cross section is:

$$\sigma = \int_0^{2\pi} \int_0^{\pi} \frac{d\sigma}{d\Omega}(\theta, \phi) \sin(\theta) d\theta d\phi \tag{2.4}$$
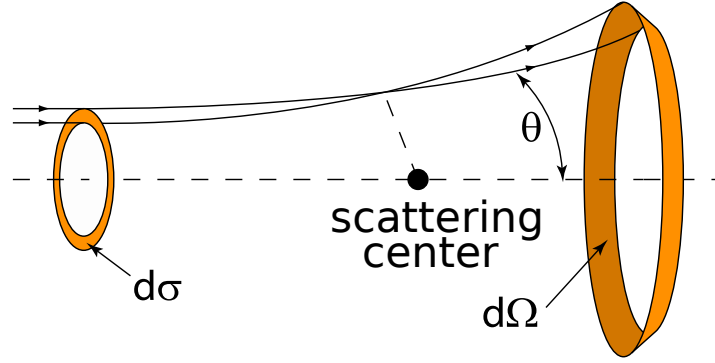
5

Figure 2.1: Diagram representing the scattering differential cross section.

In order to understand the processes involved and to give a theoretical estimate of the differential cross section of the reaction of interest, in the following sections a description of the mathematical models used to describe direct processes is presented.

Direct reactions are peripheral processes with usually low momentum transfer, among them different channels could be identified:

Elastic and Inelastic Scattering: the mass distribution of the interacting nuclei remains unaltered after reaction.

Transfer reaction: A mass rearrangement between the two species takes place.

Breakup reaction: One of the colliding partners dissociates into two or more fragments.

The final goal of reaction theory is to be able to reproduce the cross sections of these processes by mean of the solution of dynamical equations of the system.

The starting point for mathematical treatment of these three different processes is the same, requiring the solution of the time-independent Schrödinger equation [5].

2.1   Model Hamiltonian

The time independent Schrödinger equation is:

$$[H - E]\,\Psi = 0 \qquad (2.5)$$

with Ψ the wave function of the system, depending on the degree of freedom of projectile and target as well as the relative coordinate between them ($\Psi = \Psi(\boldsymbol{R}, \xi_p, \xi_t)$).

The Hamiltonian of the system can be defined as:

$$H = \hat{T}_{\boldsymbol{R}} + H_p(\xi_p) + H_t(\xi_t) + V(\boldsymbol{R}, \xi_p, \xi_t) \qquad (2.6)$$

6

$\hat{T}_{\boldsymbol{R}}$ is the kinetic energy operator ($\hat{T} = -\frac{\hbar^2}{2\mu}\nabla^2$).

$H_p(\xi_p) + H_t(\xi_t)$ are the internal Hamiltonian of projectile and target respectively.

$V(\boldsymbol{R}, \xi_p, \xi_t)$ is the projectile-target interaction potential.

Since this Hamiltonian corresponds to the entrance channel of the reaction (a mass redistribution can occurs in case of transfer or breakup processes) it is useful to distinguish between different mass partition, denoting them by Greek letters:

$$H = \hat{T}_\alpha + H_\alpha(\xi_\alpha) + V_\alpha(\boldsymbol{R}_\alpha, \xi_\alpha) \qquad (2.7)$$

$H_\alpha = H_p(\xi_p) + H_t(\xi_t)$.

ξ_α is the projectile and target coordinates in partition α.

The total energy of the system is the sum of kinetic and internal energies of the particles involved:

$$E = E_\alpha + \varepsilon_\alpha = \frac{\hbar^2 K_\alpha^2}{2\mu_\alpha} + \varepsilon_\alpha \qquad (2.8)$$

In order to solve Schrödinger Eq. 2.5 the boundary condition must be defined. The incident beam is assumed to be a plane wave, forming a set of outgoing spherical waves after the interaction with target (see Fig. 2.2).
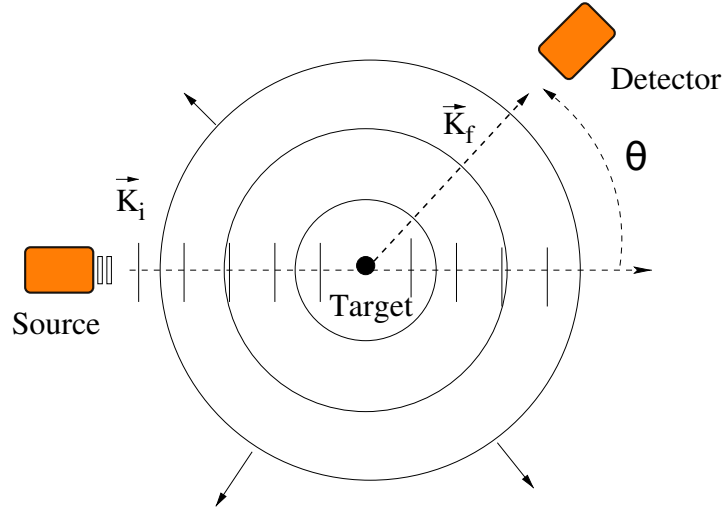

Figure 2.2: Representation of a scattering process, showing incident plane waves and outgoing spherical waves. Figure adapted from [5].

Asymptotically:

$$\Psi_{\boldsymbol{K}_\alpha}^{(+)}(\boldsymbol{R}, \xi) \rightarrow \Phi_\alpha(\xi)e^{i\boldsymbol{K}_\alpha \cdot \boldsymbol{R}_\alpha} + \text{outgoing sph. waves} \qquad (2.9)$$

$$\Phi_\alpha(\xi) = \Phi_0^{(p)}(\xi_p)\Phi_0^{(t)}(\xi_t)$$

The outgoing waves are highly distorted during the interaction, but at large distances, where the interaction term of Eq. 2.6 vanishes, the particles will emerge in any of the kinematically allowed eigenstates:

$$\Psi_{\boldsymbol{K}_\alpha}^{(+)}(\boldsymbol{R}, \xi) \rightarrow \Phi_\alpha(\xi)e^{i\boldsymbol{K}_\alpha \cdot \boldsymbol{R}_\alpha} + \Phi_\alpha(\xi_\alpha)f_{\alpha,\alpha}(\theta)\frac{e^{iK_\alpha R_\alpha}}{R_\alpha}$$

$$+ \sum_{\alpha \neq \alpha'} \Phi_{\alpha'}(\xi_\alpha)f_{\alpha',\alpha}(\theta)\frac{e^{iK_{\alpha'} R_\alpha}}{R_\alpha} \qquad (2.10)$$

$$\Psi_{\boldsymbol{K}_\alpha}^{(+)}(\boldsymbol{R}, \xi) \rightarrow \sum_{\beta \neq \alpha} \Phi_\beta(\xi_\beta)f_{\beta,\alpha}(\theta)\frac{e^{iK_\beta R_\beta}}{R_\beta} \qquad (2.11)$$

The two asymptotic solutions correspond to the elastic/inelastic scattering and transfer channel respectively. The functions $f_{\alpha,\alpha}(\theta)$, $f_{\alpha',\alpha}(\theta)$ and $f_{\beta,\alpha}(\theta)$ are the corresponding scattering amplitudes of the 3 processes. With these amplitudes it is possible to derive the differential cross section as [6]:

$$\left(\frac{d\sigma}{d\Omega}\right)_{\alpha \rightarrow \beta} = \frac{v_\beta}{v_\alpha}|f_{\beta,\alpha}(\theta)|^2 \qquad (2.12)$$

where v_α and v_β are the initial and final asymptotic velocities. Eq. 2.12 can be rewritten as:

$$\left(\frac{d\sigma}{d\Omega}\right)_{\alpha \rightarrow \beta} = \frac{\mu_\alpha \mu_\beta}{(2\pi\hbar^2)^2}\frac{K_\beta}{K_\alpha}|\tau_{\beta,\alpha}(\theta)|^2 \qquad (2.13)$$

defining the transition matrix:

$$\tau_{\beta,\alpha}(\theta) \equiv -\frac{(2\pi\hbar^2)}{\mu_\beta}f_{\beta,\alpha}(\theta) \qquad (2.14)$$

The scattering amplitude corresponding to a particular channel of interest β can be isolated left-multiplying Eq. 2.10-2.11 by the internal wavefunction of the channel ($\Phi_\beta(\xi_\beta)$) and integrating over the internal coordinates (ξ_β):

$$X_\beta(\boldsymbol{R}_\beta) \equiv (\Phi_\beta|\Psi_{\boldsymbol{K}_\alpha}^{(+)}) \rightarrow \delta_{\beta,\alpha}e^{i\boldsymbol{K}_\alpha \cdot \boldsymbol{R}_\alpha} + f_{\beta,\alpha}(\theta)\frac{e^{iK_\beta R_\beta}}{R_\beta} \qquad (2.15)$$

A formal expression of $f_{\beta,\alpha}(\theta)$ is obtained writing Schrödinger Eq. 2.5 with the proper Hamiltonian of channel β (Eq. 2.7). As done for the definition of $X_\beta(\boldsymbol{R}_\beta)$, left-multiplying and integrating over internal coordinates the following projected equation is obtained:

$$\left[\hat{T}_\beta + \varepsilon_\beta - E\right]X_\beta(\boldsymbol{R}_\beta) = -(\Phi_\beta|V_\beta|\Psi_{\boldsymbol{K}_\alpha}^{(+)}) \qquad (2.16)$$

8

$$\varepsilon_\beta = \langle \Phi_\beta(\xi_\beta)|H_\beta|\Phi_\beta(\xi_\beta)\rangle$$

The solution of this second-order inhomogeneus differential equation can be written using the Green's function in channel β $\left(G_\beta(\boldsymbol{R}_\beta, \boldsymbol{R}'_\beta) \equiv \frac{e^{iK_\beta|\boldsymbol{R}_\beta - \boldsymbol{R}'_\beta|}}{|\boldsymbol{R}_\beta - \boldsymbol{R}'_\beta|}\right)$:

$$X_\beta(\boldsymbol{R}_\beta) = \delta_{\alpha,\beta}e^{i\boldsymbol{K}_\alpha \cdot \boldsymbol{R}_\alpha} - \frac{\mu_\beta}{2\pi\hbar^2}\int G_\beta(\boldsymbol{R}_\beta, \boldsymbol{R}'_\beta)(\Phi_\beta|V_\beta\Psi^{(+)}_{\boldsymbol{K}_\alpha})d\boldsymbol{R}'_\beta \quad (2.17)$$

In the asymptotic limit $(\boldsymbol{R}_\beta \gg \boldsymbol{R}'_\beta)$ the green function become:

$$G_\beta(\boldsymbol{R}_\beta, \boldsymbol{R}'_\beta) \to \frac{e^{iK_\beta R_\beta}}{R_\beta} \quad (2.18)$$

Therefore Eq. 2.17 reduces to:

$$X_\beta(\boldsymbol{R}_\beta) \to \delta_{\alpha,\beta}e^{i\boldsymbol{K}_\alpha \cdot \boldsymbol{R}_\alpha} - \frac{\mu_\beta}{2\pi\hbar^2}\frac{e^{iK_\beta R_\beta}}{R_\beta}(\Phi_\beta|V_\beta\Psi^{(+)}_{\boldsymbol{K}_\alpha}) \quad (2.19)$$

Using Eq. 2.15 we obtain the integral equation for the scattering amplitude:

$$f_{\beta,\alpha}(\theta) =$$
$$-\frac{\mu_\beta}{2\pi\hbar^2}\int\int e^{-i\boldsymbol{K}_\beta \cdot \boldsymbol{R}_\beta}\Phi^*_\beta(\xi_\beta)V_\beta(\boldsymbol{R}_\beta, \xi_\beta)\Psi^{(+)}_{\boldsymbol{K}_\alpha}(\boldsymbol{R}_\alpha, \xi_\alpha)d\xi_\beta d\boldsymbol{R}_\beta \quad (2.20)$$

The same equation in terms of the transition matrix is:

$$\tau_{\beta,\alpha}(\theta) = \int\int e^{-i\boldsymbol{K}_\beta \cdot \boldsymbol{R}_\beta}\Phi^*_\beta(\xi_\beta)V_\beta(\boldsymbol{R}_\beta, \xi_\beta)\Psi^{(+)}_{\boldsymbol{K}_\alpha}(\boldsymbol{R}_\alpha, \xi_\alpha)d\xi_\beta d\boldsymbol{R}_\beta \quad (2.21)$$

A more general solution is given by the Gell-Mann-Goldberger transformation where an auxiliary potential $U_\beta(\boldsymbol{R}_\beta)$ is added to both sides of Eq. 2.16. The scattering matrix with this transformation is:

$$\tau_{\beta,\alpha}(\theta) = \tau^{(0)}_{\beta,\alpha}\delta_{\alpha,\beta}$$
$$+ \int\int \chi^{(-)*}_\beta(\boldsymbol{K}_\beta, \boldsymbol{R}_\beta)\Phi^*_\beta(\xi_\beta)\left[V_\beta - U_\beta\right]\Psi^{(+)}_{\boldsymbol{K}_\alpha}(\boldsymbol{R}_\alpha, \xi_\alpha)d\xi_\beta d\boldsymbol{R}_\beta \quad (2.22)$$

The function $\chi^{(-)}_\beta(\boldsymbol{K}_\beta, \boldsymbol{R}_\beta) = \chi^{(+)*}_\beta(-\boldsymbol{K}_\beta, \boldsymbol{R}_\beta)$ is the conjugate solution of the homogeneous equation:

$$\left[\hat{T}_\beta + U_\beta + \varepsilon_\beta - E\right]\chi^{(+)}_\beta(\boldsymbol{K}_\beta, \boldsymbol{R}_\beta) = 0 \quad (2.23)$$

Eq. 2.22 is an exact solution to the scattering problem, but cannot be solved because it contains the exact wave-function of the system $\Psi^{(+)}_{\boldsymbol{K}_\alpha}(\boldsymbol{R}_\alpha, \xi_\alpha)$, therefore an approximation is necessary.

2.2 DWBA

The specific case analyzed in this work is a transfer reaction, where projectile and target exchange one or more nucleons. Using the coordinates of the final configuration (see Fig. 2.3) the Hamiltonian of Eq. 2.6 become:

$$H = \hat{T}_{\boldsymbol{R'}} + H_B(\xi', \boldsymbol{r'}) + H_a(\xi) + V_{bx} + U_{bA} = \hat{T}_{\boldsymbol{R'}} + H_\beta(\xi_\beta) + V_\beta(\boldsymbol{R'}, \boldsymbol{r'}) \quad (2.24)$$
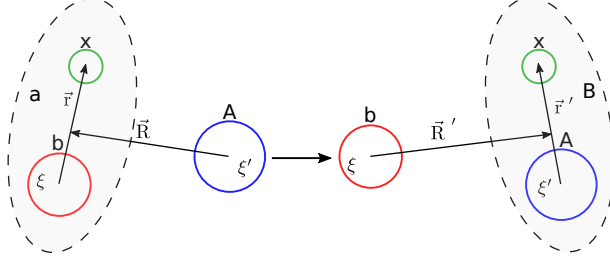
Figure 2.3: Transfer reaction showing the initial and final coordinates reference system. Figure adapted from [5].

Gell-Mann-Goldberger Eq. 2.22 can be rewritten in the case of a transfer reaction as:

$$\tau_{\beta,\alpha}(\theta) = \int \int \chi_\beta^{(-)*}(\boldsymbol{K'}, \boldsymbol{R'}) \Phi_\beta^*(\xi_\beta) \left[V_\beta - U_\beta\right] \Psi_{\boldsymbol{K}}^{(+)}(\boldsymbol{R}, \xi_\alpha) d\xi_\beta d\boldsymbol{R'} \quad (2.25)$$

$\Psi_{\boldsymbol{K}}^{(+)}(\boldsymbol{R}, \xi_\alpha)$ is the exact wave-function of the system.
$\Phi_\beta^*(\xi_\beta)$ is the internal wave-function of the final nuclei, and satisfy:

$$H_\beta \Phi_\beta(\xi_\beta) = \varepsilon_\beta \Phi_\beta(\xi_\beta) \text{ with } \Phi_\beta(\xi_\beta) = \phi_b(\xi)\phi_B(\xi', \boldsymbol{r'}) \quad (2.26)$$

The DWBA (Distorted Wave Born Approximation) method consists in the approximation of the exact wave-function as:

$$\Psi_{\boldsymbol{K}}^{(+)}(\boldsymbol{R}, \xi_\alpha) \sim \chi_\alpha^{(+)}(\boldsymbol{K}, \boldsymbol{R})\Phi_\alpha(\xi_\alpha) \quad (2.27)$$

$\Phi_\alpha(\xi_\alpha) = \phi_a(\xi, \boldsymbol{r})\phi_A(\xi')$
where $\chi_\alpha^{(+)}(\boldsymbol{K}, \boldsymbol{R})$, related to projectile-target relative motion in the entrance channel, is the solution of the homogeneous equation:

$$\left[\hat{T}_{\boldsymbol{R}} + U_\alpha + \varepsilon_\alpha - E\right] \chi_\alpha^{(+)}(\boldsymbol{K}, \boldsymbol{R}) = 0 \quad (2.28)$$

The auxiliary potential U_α is usually chosen to reproduce elastic scattering differential cross section.

The final DWBA scattering amplitude can be written as:

$$\tau_{\beta,\alpha}^{\text{DWBA}}(\theta) = \int\int \chi_\beta^{(-)*}(\boldsymbol{K}',\boldsymbol{R}')\Phi_\beta^*(\xi_\beta)\left[V_\beta - U_\beta\right]\chi_\alpha^{(+)}(\boldsymbol{K},\boldsymbol{R})\Phi_\alpha(\xi_\alpha)d\xi_\beta d\boldsymbol{R}'$$
(2.29)

Considering the specific case analyzed in this work, a (d,p) transfer reaction, the interaction potential V_β is given by $V_\beta = V_{pn} + U_{pA}$. A further approximation is $U_{pA} \sim U_{pB}$ which gives $V_{pn} + U_{pA} - U_{pB} \sim V_{pn}$ (the amplitude is dominated by p-n interaction). The internal states and coordinates are given by:

$$\Phi_\alpha(\xi_\alpha) = \varphi_d(\boldsymbol{r})\phi_A(\xi')$$
(2.30)
$$\Phi_\beta(\xi_\beta) = \Phi_B(\xi',\boldsymbol{r}')$$
(2.31)

Finally the DWBA scattering amplitude for this specific process becomes:

$$\tau_{d,p}^{\text{DWBA}}(\theta) =$$
$$\int\int \chi_p^{(-)*}(\boldsymbol{K}_p,\boldsymbol{R}')\Phi_B^*(\xi',\boldsymbol{r}')V_{pn}(\boldsymbol{r})\chi_d^{(+)}(\boldsymbol{K}_d,\boldsymbol{R})\varphi_d(\boldsymbol{r})\phi_A(\xi')d\xi_\beta d\boldsymbol{R}' \quad (2.32)$$

The overlap integral between target and residual nuclei functions (see Eq. 2.33) is not straightforward because it requires the knowledge of the many-body wave function of the two nuclei.

$$\varphi_{An}(\boldsymbol{r}') = \int \Phi_B^*(\xi',\boldsymbol{r}')\phi_A(\xi')d\xi'$$
(2.33)

It is customary to approximate $\varphi_{An}(\boldsymbol{r}')$ with a single particle neutron wavefunction relative to the residual nucleus core, weighted by a coefficient C_{An}^B called spectroscopic amplitude:

$$\varphi_{An}(\boldsymbol{r}') \rightarrow C_{An}^B \widetilde{\varphi}_{An}^{\,ljI}(\boldsymbol{r}')$$
(2.34)

where I is the core A spin, l the orbital angular momentum and j the total momentum sum of l and intrinsic spin s. With this final approximation the differential cross section of the process can be computed as:

$$\frac{d\sigma}{d\Omega}_{d,p}(\theta) =$$
$$\frac{\mu_\alpha\mu_\beta}{(2\pi\hbar^2)^2}S_{An}^B\left|\int\int \chi_p^{(-)*}(\boldsymbol{K}_p,\boldsymbol{R}')\widetilde{\varphi}_{An}^{\,ljI}(\boldsymbol{r}')^*V_{pn}(\boldsymbol{r})\chi_d^{(+)}(\boldsymbol{K}_d,\boldsymbol{R})\varphi_d(\boldsymbol{r})d\boldsymbol{r}'d\boldsymbol{R}'\right|^2$$
(2.35)

where $S_{An}^B \equiv \left|C_{An}^B\right|^2$ is called Spectroscopic Factor. It can be understood as the occupation number of the orbital $l\,j$ with the core A in the given state I.

11

A large SF means a strong population of single particle states in the residual nucleus. It is important to underline that SF is not a direct observable of an experiment, it is model-dependent and it is extracted comparing the theoretical and experimental differential cross sections giving information on the collectivity or single particle behavior of nuclei.

The two differential cross sections computed with the DWBA method for $l = 0$ and $l = 2$ transfers are reported in Fig. 2.4. The effective local potential for d+^{16}O was obtained by using the energy dependent global optical potential from [7]. The distorting potential governing the center of mass motion of the deuteron is well described by the sum of the neutron/proton-target optical potentials, parametrized in [8]. Finally the fundamental state of deuterium and the states of ^{17}O were described with a Gaussian and a Wood-Saxon potential respectively.
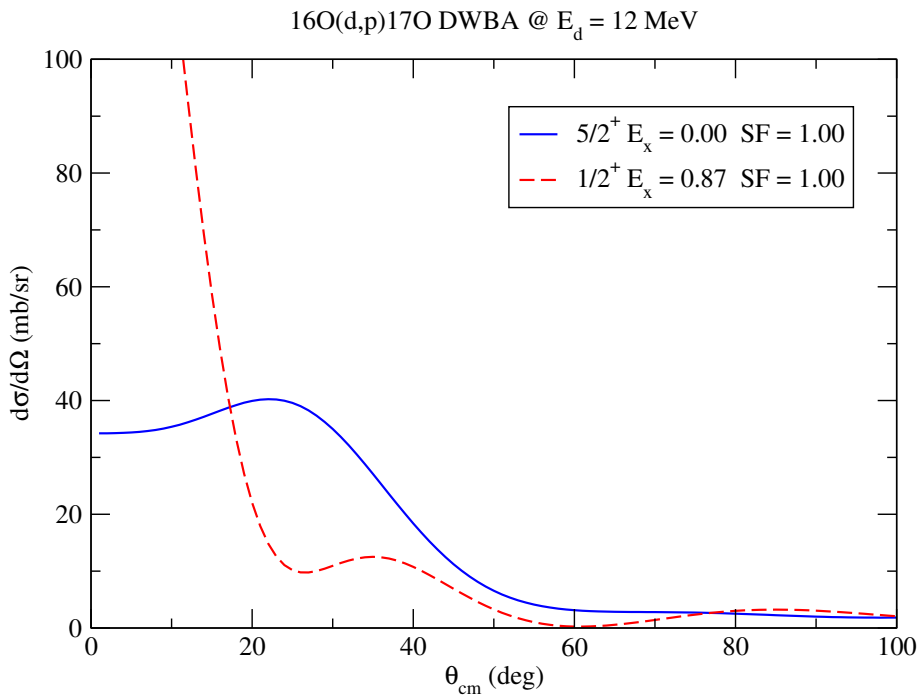
Figure 2.4: DWBA diffrential cross section for the $l = 0$ and $l = 2$ neutron transfer. Calculation performed by Jesus Casal, INFN-Padova Section.

3 Experimental Setup

In this chapter the experimental setup tested for the first time with this commissioning experiment is described. The apparatus is located in the G1 experimental room of GANIL (see Fig. 3.1) where VAMOS spectrometer is placed. It consists of three different detection units, each one dedicated to a specific task:

AGATA (Advanced GAmma Tracking Array) is an HPGe array dedicated to the detection of gamma-ray decay of the excited nuclei.

MUGAST (MUst2 GASpard Trace) Silicon array is used to detect the light charged recoil ejectiles of the reaction.

VAMOS (VAriable MOde Spectometer) magnetic spectrometer is intended to detect and reconstruct the trajectory of heavy outgoing nuclei strongly focused at forward angles.
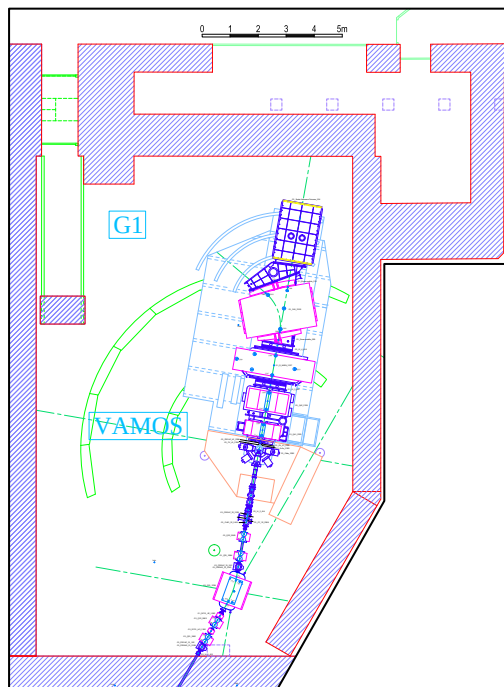
Figure 3.1: G1 experimental hall layout at GANIL showing VAMOS spectometer, AGATA and MUGAST are not present in this figure.

Using as reference the commissioning reaction d(^{16}O,^{17}O)p, the outgoing protons are therefore detected by MUGAST array measuring their energy and angle in the laboratory reference system. These two quantities allow the reconstruction of ^{17}O excitation energy, while the eventual gamma ray emitted by the populated $1/2^+$ level is detected by AGATA, granting an additional information on nuclear state with an higher resolution. Finally ^{17}O is detected by VAMOS spectrometer, measuring its kinematic information such as charge state, β and emission direction. The information acquired by the three systems grant a complete view over the reaction with an increased efficiency and resolution compared to other setup.

3.1   AGATA

A powerful method to study nuclei structure is direct detection, at high energy resolution, of gamma rays emitted from the de-excitation processes of nuclear levels.

Gamma rays interact with matter with three different mechanisms depicted in Fig. 3.2, depending on their energy and absorber atomic number. Photoelectric effect happens when a gamma ray is completely absorbed by a medium atom and a consequent photo-electron is emitted with energy $E_{e^-} = h\nu - E_b$ where E_b is the binding energy of the atomic electron. It is dominant at lower energies and its cross section increases with medium atomic number.

At intermediate energies Compton effect is the relevant process, in this case the incident radiation is not completely absorbed, emitting a scattered gamma ray and a recoil electron. Energy of the scattered radiation is ruled by energy and momentum conservation law:

$$E_{\gamma'} = \frac{h\nu_0}{1 + (h\nu_0/m_{e^-}c^2)(1 - \cos(\theta))} \tag{3.1}$$

where $h\nu_0$ is the energy of the original gamma ray and θ the scattering angle of the outgoing gamma ray. The angular distribution of Compton scattered gamma rays is ruled by Klein–Nishina differential cross section:

$$\frac{d\sigma}{d\Omega}(\theta) = \frac{r_e^2}{2} \left(\frac{h\nu_f}{h\nu_i} \right)^2 \left(\frac{h\nu_f}{h\nu_i} + \frac{h\nu_i}{h\nu_f} - \sin^2(\theta) \right) \tag{3.2}$$

When radiation energy exceeds 1.022 MeV an electron-positron pair can be generated with the so called Pair production. Due to momentum conservation this can only happen in the presence of an atomic medium.
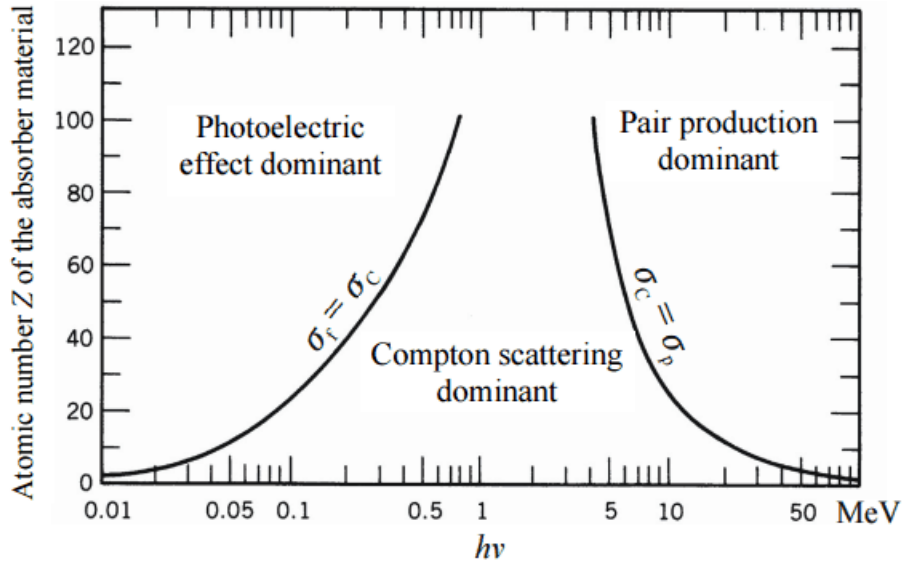
Figure 3.2: Gamma ray interaction mechanisms at different energies and absorber atomic numbers.

These mechanisms ruled detectors development with the final purposes of gain efficiency and resolution. Germanium semiconductor detectors are the best in latter terms and important results were obtained during the last decades in their development.

Different configuration are used (see Fig. 3.3) in order to reduce the Compton background due to gamma rays escaped from the detection system. Compton shielded Germanium arrays such as GALILEO [9] at LNL use high efficiency BGO detectors to surround the crystals and reject Compton scattered gamma rays outside the Germanium detector. This increases the P/T ratio but causes a loss in efficiency due to the solid angle covered by the shield. The use of only conventional Germanium detectors would requires to many crystals in order to avoid summing effects and maintain a good resolution, therefore the solution are Germanium segmented tracking arrays. Other than having an optimal solid angle coverage and P/T ratio, boost in angular resolution is obtained, fundamental for Doppler correction of gamma ray emitted in-flight.
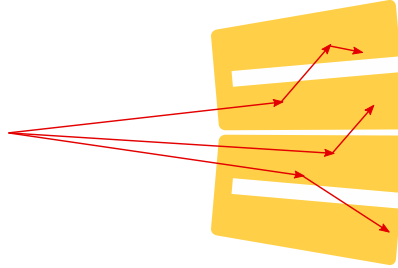
Compton Shielded Ge

Ph. Ɛ ~ 10%
P/T ~ 60%
θ res. ~ 8 deg
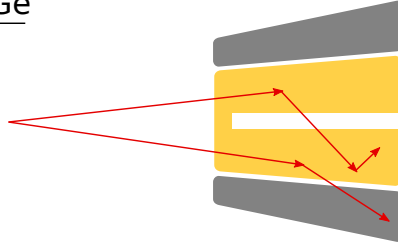
Ge Sphere

Ph. Ɛ ~ 50%
P/T ~ 30%
θ res. ~ 3 deg

Ge Tracking Array
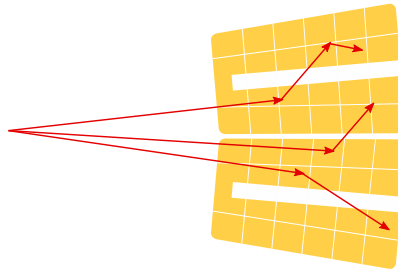
Ph. Ɛ ~ 50%
P/T ~ 60%
θ res. ~ 1 deg

Figure 3.3: The different Germanium detector arrays configurations and their indicative performances.

In this sense AGATA [10] is the state of the art of HPGe gamma ray tracking arrays. It is the result of an European collaboration, supported by the funding of several agencies, aiming to build a 4π array. Currently the project is reaching the 1π configuration, equipped with 47 crystals divided in triple clusters. Each crystal is segmented in 6 rings of 6 segments each, for a total of 36 segments and a central core (see Fig. 3.4). The hexagonal geometry of the crystals was chosen to maximize the active volume in the final array, while the increasing thickness of the rings is adopted to compensate the counting rate at different depths inside the detector. The low energy band gap of Germanium ($\sim$4 eV at 300 K) provide a very good energy resolution, but requires the cooling of the semiconductor at $\sim$ 90 K. This is obtained via a cooling finger in contact with liquid Nitrogen contained in a dewar.
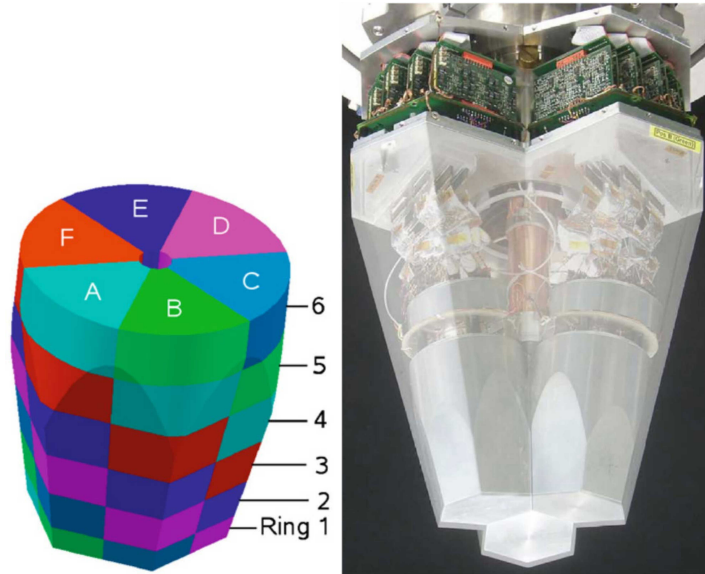
Figure 3.4: Crystal segmentation diagram (left) and final encapsulated triple cluster (right).

AGATA is intended to work with digital electronics, therefore the signals produced by the preamplifier are sent to dedicated 100-MHz 14-bit ADC units. The digitized information are preprocessed by FPGA electronics to generate fast-logic signals for hardware trigger and reducing data volume from the digitizers of a factor 100. Filtered data are finally sent to the acquisition farm.

The peculiarity of AGATA is the implementation of two different algorithms to gain a position sensitivity of 5 mm and reconstruct multiple interaction points belonging to the same original gamma ray: Pulse Shape Analysis (PSA) and tracking algorithm.

3.1.1 Pulse Shape Analysis

In a coaxial Germanium detector, just as in other detectors where charge carriers are collected by the electrodes over appreciable distances, the shapes of generated pulses have a radial dependence on interaction position [11]. Furthermore the intrinsic presence of cross-talk between segments generates induced charges on the neighbouring electrodes (see Fig. 3.6). Combining this two effects is possible to achieve a 5 mm position resolution for gamma-ray interaction inside the crystal better than the segment characteristic dimensions, of the order of some centimeters. The algorithms devoted to PSA rely on the comparison of segment signals recorded during a gamma-ray event with a base of reference signals. These are obtained from each crystal either via scanning systems, based on collimated sources, or simulated signal shapes database.
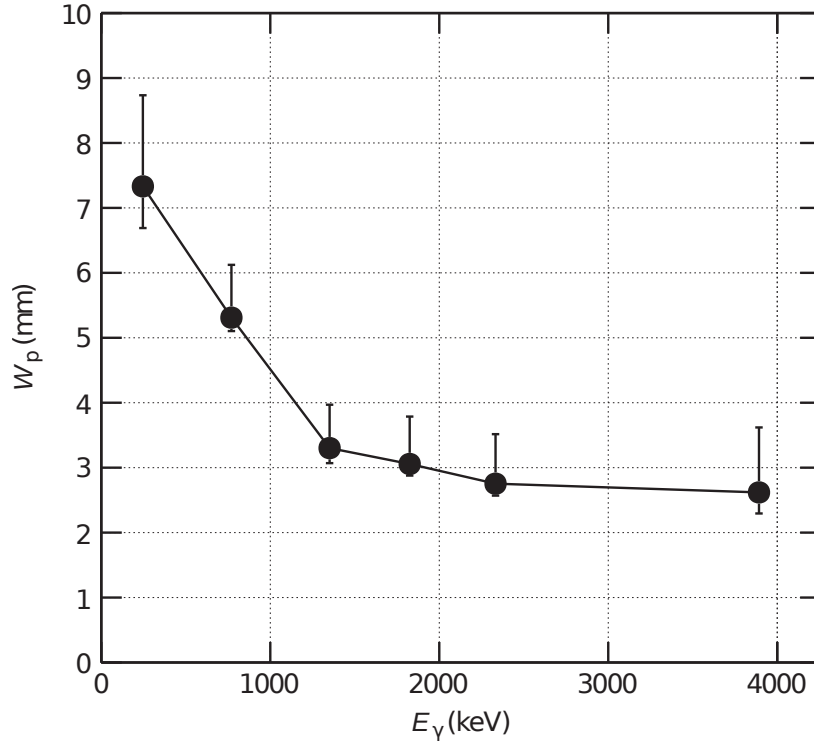
Figure 3.5: Interaction position resolution as a function of gamma-ray energy extracted from the first AGATA in-beam commissioning at LNL. Fig. adapted from [10].
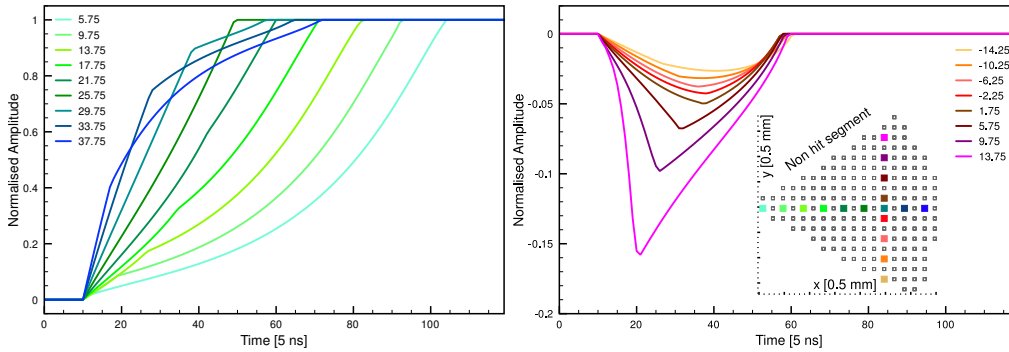

Figure 3.6: Core signals for simulated interaction at different radial distances (left) and non-hit neighbouring segment induced signals (right). The diagram on the right shows the color scheme for different interaction positions inside the segment. Fig. adapted from [12].

3.1.2 Tracking

The final processing phase of the data coming from an AGATA crystal is the tracking filter. A correct reconstruction of gamma ray interaction path inside the detector (see Fig. 3.7) is fundamental to increase the P/T ratio reducing Compton background. In this direction several algorithms were developed, the most commonly used is forward tracking, which is implemented in two versions: MGT (Mars Gamma-ray Tracking) [13] and OFT (Orsay Forward Tracking) [14]. The first step of the tracking is a clusterization of the interactions, based on progressive angular aperture and number of points. Each cluster is then evaluated by assigning a merit factor based on path length of gamma rays inside the Germanium crystal, Photo electric cross section for the last presumed hit and likelihood of Compton scattering based on kinematic relation between scattering angle and gamma ray energy. The algorithm finally sorts the clusters requiring that the merit factor is greater than two tunable parameters: *minprobsing* for single interaction points and *minprobtrack* for the cluster.
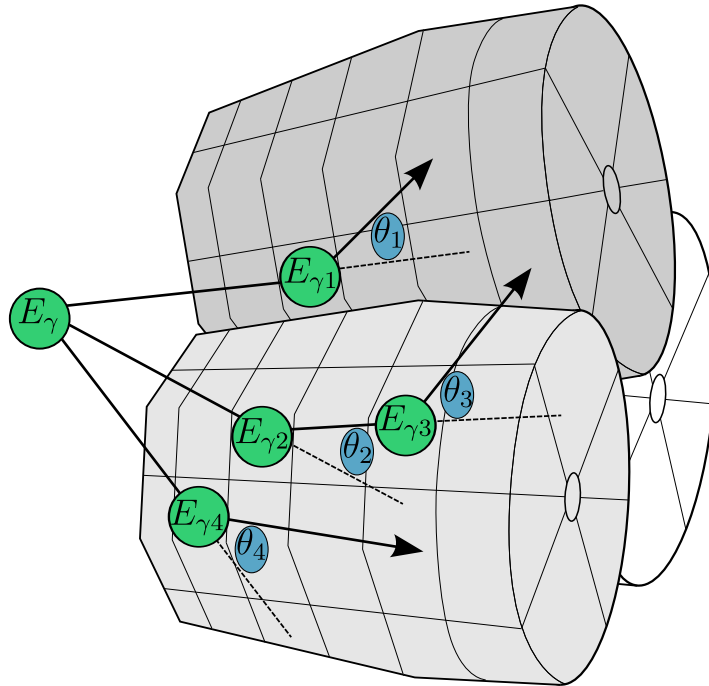

Figure 3.7: Schematic picture of a gamma-ray tracking reconstruction inside an AGATA triple cluster. Fig. adapted from [15].

3.2 MUGAST

Direct reactions are a great tool to investigate Exotic Nuclei and Astrophysical processes. In this sense, with the advent of radioactive ion beams a new window of possibilities was opened, especially with the use of inverse kinematic reactions. A precise detection of recoiling light particles is however needed to extract the desired information. Silicon semiconductor detectors are the best choice, in fact, due to their limited dimensions, can be placed inside the reaction chamber. This is fundamental as, differently from gamma ray, charged particles would be stopped outside vacuum chamber. The angular coverage and resolution are another important requirement. The emission angles depicted in Fig. 3.8 for transfer reactions strongly depends on differential cross section and kinematic of the processes, therefore a wide coverage of the solid angle is a desiderable characteristic for a Silicon array setup. Angular resolution, instead, is needed for precise reconstruction of excitation energy of produced nuclei.
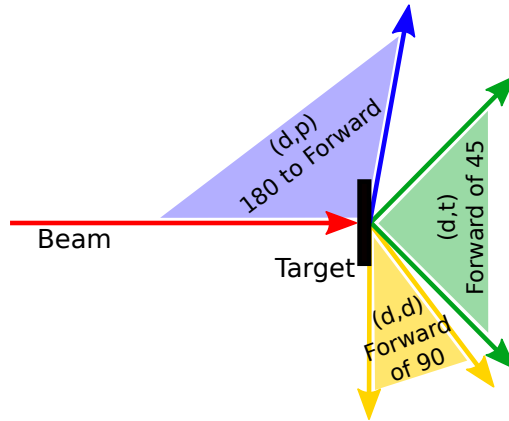

Figure 3.8: Schematic representation of angular coverage for different transfer reactions performed in inverse kinematic.

The evolution of this approach starts from MUST [16] and its upgrade MUST2 [17] silicon telescopes, specifically designed for particle spectroscopy. The limitation of these systems remains however the dimension due to the multilayer technology and the poor resolution achievable in terms of excitation energy due to energy straggling inside target thickness. In the last years GRIT project, a new collaboration between several European research groups, was created. The aim is the production of next generation Silicon array with a 4π configuration and specifically designed to be coupled with gamma-ray detector arrays such AGATA and cryogenic target such CHyMENE (see Fig. 3.9-(a)). This feature allows to increase excitation energy resolution up to a factor $\sim$100 thanks to the high resolution HPGe gamma-ray detectors while the use of windowless cryogenic targets, in the

case of light mass nuclei such Hydrogen and Helium isotopes, provide the highest purity and the absence of energy straggling due to the presence of Havar windows.

MUGAST setup (see Fig. 3.9-(b)), used in this commissioning experiment, is an intermediate configuration of the GRIT project, making use of the high granularity silicon arrays of GASPARD-TRACE collaborations and 4 MUST2 telescopes.
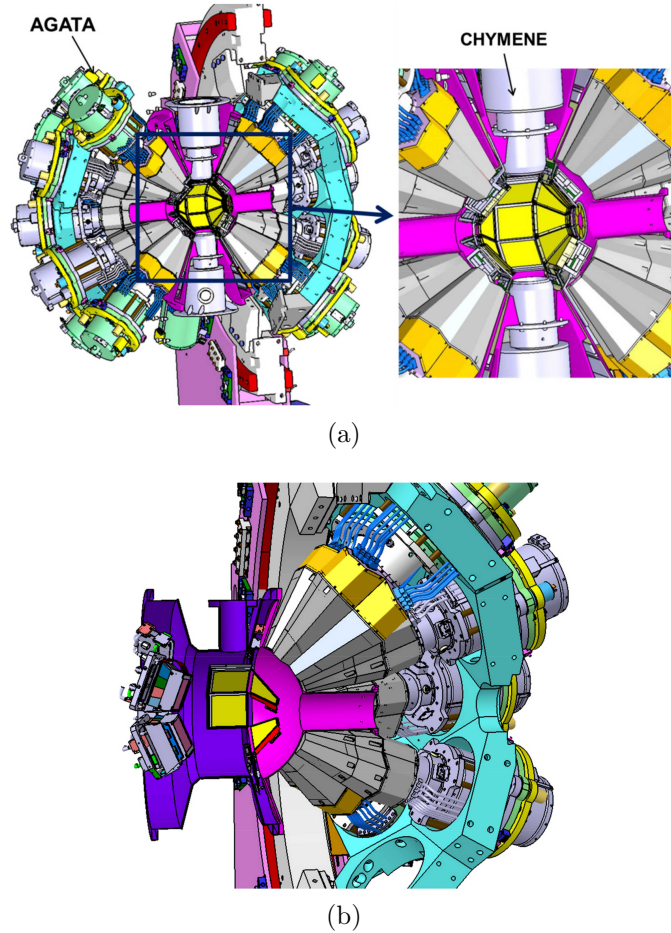

(a)

(b)

Figure 3.9: GRIT Silicon array inside the final full AGATA configuration with the cryogenic CHyMENE target (a) and MUGAST commissioning setup (b).

3.2.1 MUGAST DSSD

The working principle behind Silicon detectors is the same of Germanium semiconductor detectors. A wafer of Silicon is p-n doped on the two sides, forming a junction in the middle. If inversely polarized with a voltage power supply a large depletion region is formed. A ionizing particle hit-

ting the detector will form a track of $h^+ - e^-$ pairs which drifts towards the respective electrodes, inducing a measurable current on them. A set of different shape DSSD (Double-sided Silicon Strip Detector) are used, where the doping on the two sides is created as electrically separated strips perpendicularly oriented. The junction is formed between the p and n perpendicular strips, allowing to reconstruct the interaction position with the coincidence between $h^+ - e^-$ induced signals and a position resolution equal to half the strip spacing (see Fig. 3.10-(a)).

The DSSD used are organized as follow:

- 1 Annular detector located at the most backward angles in the laboratory reference system (300 μm thick).

- 5 Trapezoidal shape detectors (see Fig. 3.10-(b)) in the backward hemisphere at 15 cm from target (450-500 μm thick).

- 2 Squared shape DSSD at 90 degree with respect to beam direction and at 8 cm from target (500 μm thick).

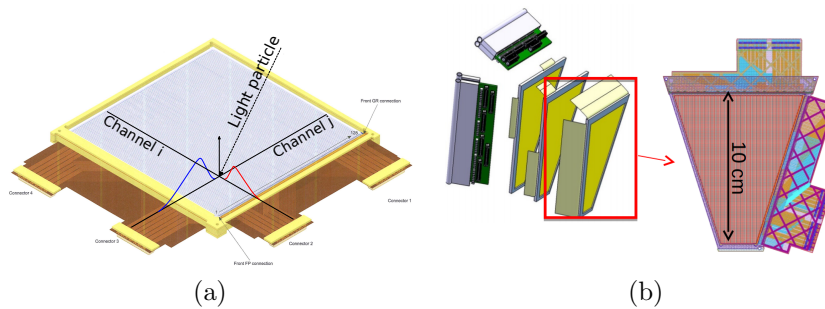(a)   (b)

Figure 3.10: Square DSSD showing the signal induced on the two perpendicular strips (a) and Trapezoidal detector scheme (b).

The trapezoidal and square detectors have 128 strip for each side while the Annular detector is divided in 16 angular sector and 64 radial rings as depicted in Fig. 3.11. Integrated digital electronics for large number of channels is not yet available, thus the electronics of MUST2 were used instead to acquire energy and time information from each detectors.

During the experiment the two square detectors were unplugged because of electronic noise problems, therefore the data analysis described in the following chapter relies only on the trapezoids and MUST2 telescopes. This unfortunately lead to the impossibility of renormalize angular distributions using elastic scattering reaction, which is peaked at 90 degree, and therefore to have an absolute value for the cross section.
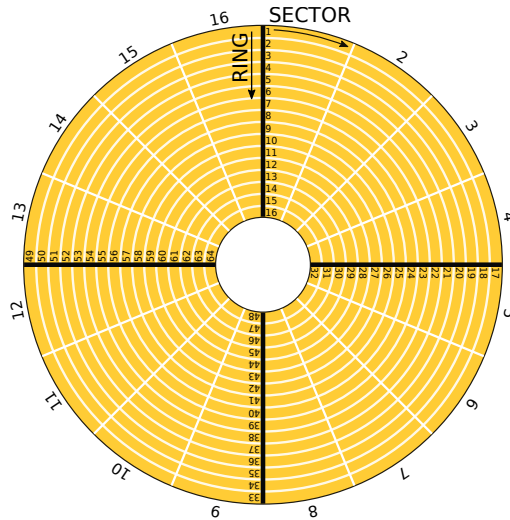
22

Figure 3.11: Annular detector layout showing the 16 angular sectors and 64 rings divided in quarters.

3.2.2 MUST2

As above mentioned, 4 MUST2 telescopes are used in the MUGAST setup. They are placed at forward angles at 17 cm from target position. Each module is composed by a square 300 μm DSSD of 10 cm side with $128{\times}128$ strips. The second layer is a CsI scintillator segmented in 16 square pads and coupled with photodiodes (see Fig. 3.12). The readout electronics for the whole MUGAST array is composed of 11 pairs of MUFEE front end cards, each one reading 128 channel (one DSSD side), computing energy and timing of the signals. The information are collected by 3 MUVI back end card of VXI type and sent to the GANIL DAQ for the acquisition.
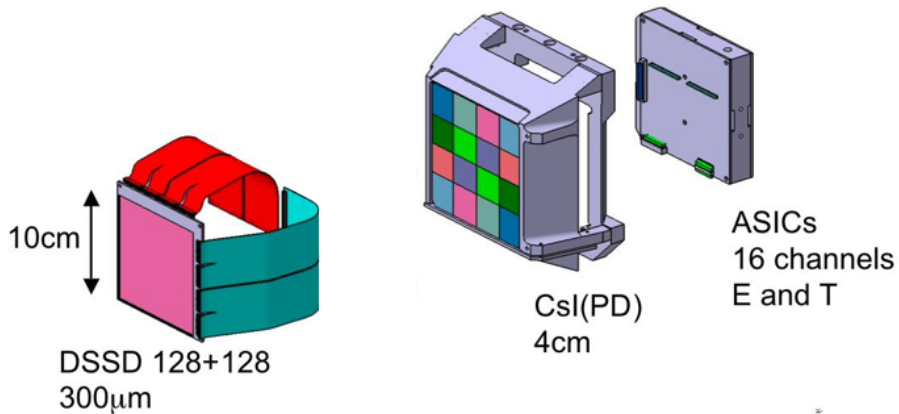

Figure 3.12: MUST2 telescope scheme showing the DSSD front layer and CsI scintillator.

23

3.3 VAMOS

VAMOS is a ray-tracing magnetic spectrometer used to identify the strongly forward focused heavy particles using the information measured on the focal plane detectors [18]. Fig. 3.13 presents a schematic drawing of the apparatus, which is composed of two large aperture quadrupoles and a magnetic dipole. The features of the spectrometer are reported in Tab. 3.1.

Horizontal acceptance	-125 mrad to 100 mrad
Vertical acceptance	± 160 mrad
M/q resolution	$\sim 0.6\%$
Maximum rigidity	1.6 Tm

Table 3.1: VAMOS characteristic features.

The working principle behind the system is to deflect ions accordingly to their magnetic rigidity $B\rho = mV/q$. The focal plane detectors consists of a MWPPAC (Multi Wire Parallel Plate Avalanche Counter) used for TOF and position measurements after the magnetic dipole, a pair of position sensitive DC (Drift Chamber) necessary to measure the ions direction and a segmented IC (Ionization Chamber) for particles identification.

An entrance MWPC (Multi Wire Proportional Counter) before the quadrupole lenses was placed to be used as start for TOF measurements and initial direction reconstruction, but it was later removed because of the energy straggling introduced. The direction and position on focal plane are used to determine the original direction of nuclei at the entrance of the apparatus through a polynomial relationship extracted by a mapping of the magnetic field inside the quadrupoles and dipole.

In the analysis process, described in the following chapter, the data acquired from VAMOS were not used. During the commissioning large part of the beam time was dedicated to fix unexpected issues of the apparatus, thus the efficiency of the system was not as expected during the statistical runs. Further studies will be needed to fully characterize the magnetic spectrometer and include it in the analysis.
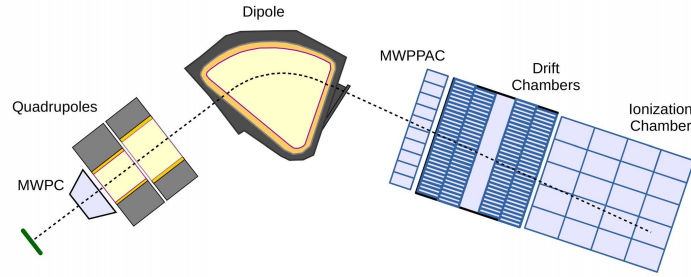
Figure 3.13: Schematic representation of VAMOS showing the magnetic quadrupoles, dipole, and the focal plane detectors. Figure adapted from [19].

3.3.1 MWPPAC

The MWPPAC is particulary suitable for TOF and position measurements thanks to its very good timing resolution. It consists of a central cathode and two anodes separated by 2.2 mm. The former is a set of vertical gold coated tungsten 20 μm wires with a pitch of 500 μm. The latters instead are a set of horizontal wires with 1 mm pitch. Position is measured through a delay line between the wires, detecting the time difference at the two sides. The detector is operated with Isobutane at ∼6 mbar, separating the chamber with 0.9 μm Mylar windows.

3.3.2 Drift Chamber

The DC, with an active volume 1000×150×100 mm^3, consists of a drift gap of 150 mm and an amplification gap of 20 mm separated by a Frisch grid of gold coated tungsten 50 μm wires as depicted in Fig. 3.14. Cathode plane is formed of two rows of 160 pads each. The direction of the particle is obtained fitting the charge distribution on consecutive pads rows. As MWPPAC the chamber is filled with Isobutane.

3.3.3 Ionization Chamber

The last section of focal plane detectors is a Ionization Chamber of 1000×120×150 mm^3 filled with CF$_4$ at typical pressures of 20-40 mbar. It is divided in 6 section along particles direction, each one subdivided in five pads. The detection principle is the same of the DC, but in this case the information is the energy loss of the ions. Comparing the energy measured by the different segments with the total energy E-ΔE identification can be applied.
The data are acquired, as for MUGAST array, by GANIL DAQ system and encapsulated in MFM format, before being sent to NARVAL merger as described in the following chapter.
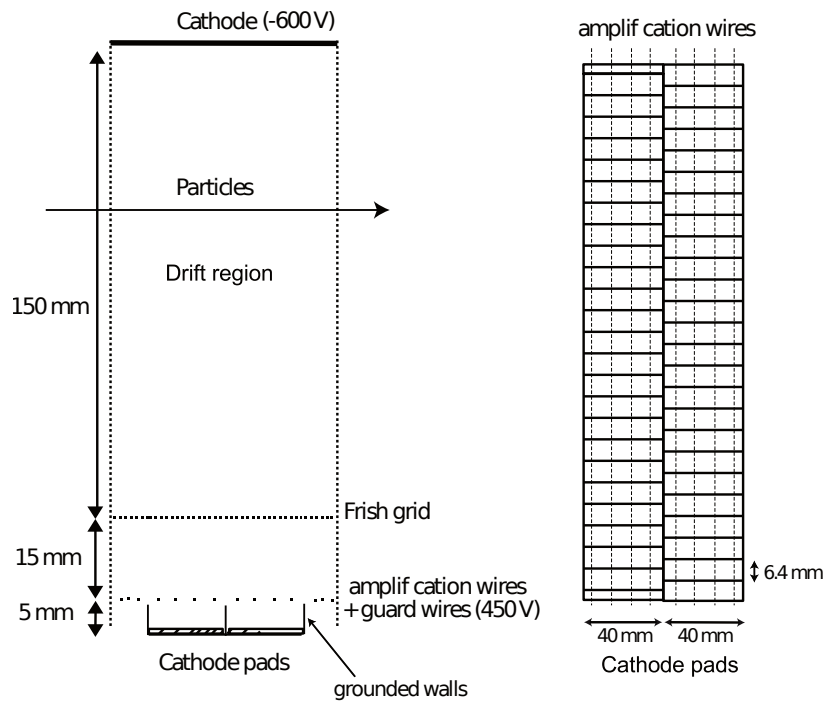
25

Figure 3.14: Drift chamber of VAMOS, showing the schematic side (left) and top (right) view of the detector. Figure adapted from [18].

4 Data Analysis

In this chapter, the analysis performed on the acquired data of the commissioning experiment is reported and discussed.

The first section is dedicated to presorting and calibration procedures, a key aspect for a correct interpretation of the information gathered from the experiment.

A simulation of reaction and MUGAST array is then carried out to compute its angular efficiency, necessary to renormalize the angular distribution of the light ejectiles detected with the silicon array.

The angular distributions of $l = 0$ and $l = 2$ transfer reactions to the $1/2^+$ (870.73 keV) and $5/2^+$ (g.s.) levels of ^{17}O are extracted and compared to the theoretical differential cross sections.

Finally, exploiting the gamma-proton coincidence, an estimate of AGATA efficiency is computed.

4.1 Presorting and Calibration

4.1.1 AGATA

AGATA data are acquired with NARVAL [20], a data acquisition system designed to manage the data flow using a chain of different actors, each one dedicated to a specific task in the data preprocessing. The system is designed to shape the information starting from the raw digitized traces till the merge with data coming from ancillary detectors. The whole process, depending on the disk saved data, can be replayed offline with FEMUL (Flat EMULator), a framework in charge of organizing the processing of data by different actors. The replay is an essential step to reach the best possible quality in the analysis process, by tuning the several parameters involved.

AGATA data flow topology is divided in two main sections, the LLP (Local Level Processing) and GLP (Global Level Processing) as shown in Fig. 4.1.
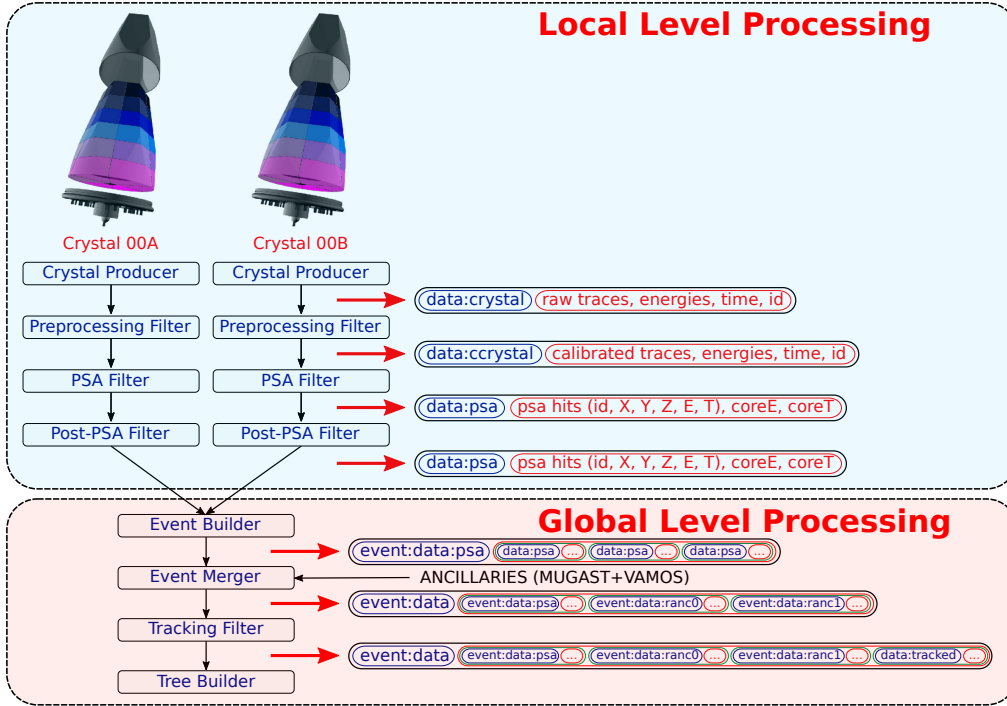
Figure 4.1: AGATA data flow topology with NARVAL system.

The former contains actors which process data coming from each crystal of the array:

- **Crystal Producer**: Starts NARVAL chain, getting the raw traces from the front end electronics and encapsulating them in the ADF (Agata Data Format) containers.

- **Preprocessing Filter**: Prepares data for PSA algorithm, applying a trapezoidal filter to calculate energy of the signals and measuring their timing. At this stage a first energy calibration is performed, together with a cross talk correction and time alignment of crystal segments.

- **PSA Filter**: Extracts from the signal shapes the position of each interaction point with a 5 mm precision.

- **Post-PSA Filter**: Performs the final operations on local level data, applying the neutron damage correction and final energy calibration.

The GLP frame contains the actors which merge data coming from different crystals and ancillary detectors:

- **Event Builder**: Builds AGATA events inside a given time window.

28

- **Event Merger**: Merges AGATA events with the ancillaries ones inside a given time window.

- **Tracking Filter**: Applies the desired tracking algorithm to the data.

- **Tree Builder**: Stores data in final Root TTree format.

The tuning of the different LLP filters was performed the days before the experiment, in order to have the possibility to analyze the data online during the acquisition, a key feature to check the ongoing experiment, particularly in a commissioning one.

Although already tuned, during offline analysis data were replayed starting from Post PSA filter. This step was necessary to correct eventual not properly calibrated segments to achieve the best resolution possible.

Post PSA filter, in detail, perform 4 operations. The first action is a linear recalibration of segments and core energies coming from the previous actor, using the spectra obtained from a ^{60}Co source with two characteristic gamma-ray energies of 1173.2 keV and 1332.5 keV. The core of Post PSA actor is neutron damage correction. Fast neutrons coming from deep inelastic collisions and fusion evaporation reactions are well known to produce lattice defects in Germanium crystals. These defects act as charge collection centers, thus reducing the efficiency of the detector. The crystal can recover from this kind of damage through an annealing process, impractical to be performed between consecutive experiments or acquisition runs. Nevertheless, a correction can be applied afterwards knowing the PSA position of interaction [21], since this phenomena depends in first approximation on interaction point inside the crystal. Fig. 4.2-4.3 report the effects of neutron damage correction applied on crystals A B and C of cluster 14 with a ^{60}Co spectrum.
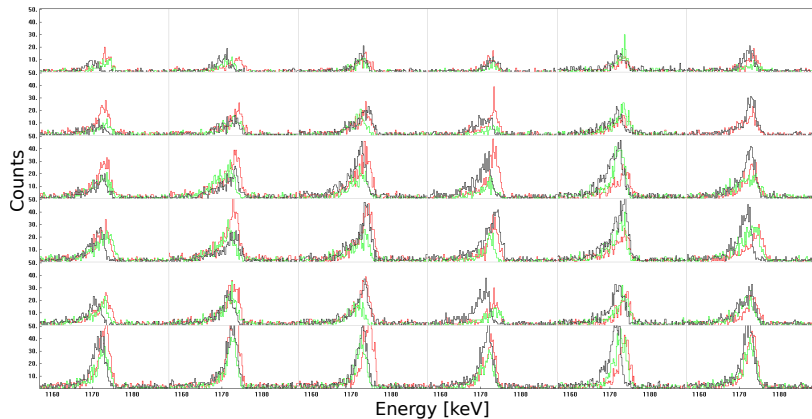

Figure 4.2: ^{60}Co 1173.2 keV peak obtained from crystals A B C of cluster 14 before neutron damage correction.
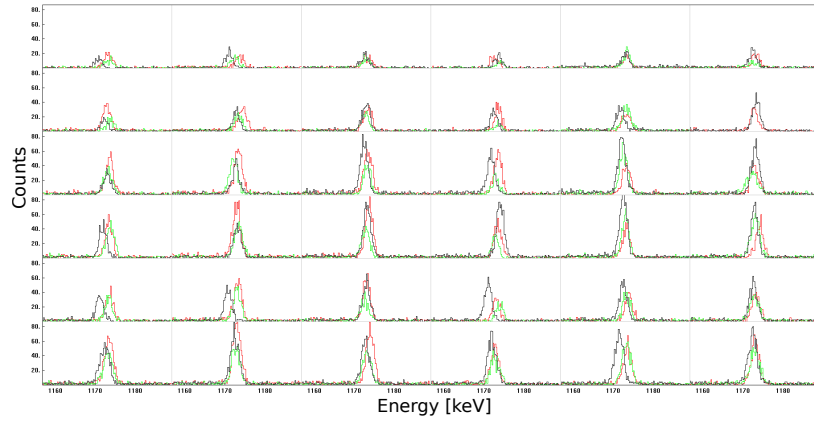
Figure 4.3: ^{60}Co 1173.2 keV peak obtained from crystals A B C of cluster 14 after neutron damage correction. The left tail of the peaks disappears, but a recalibration is necessary.

After this procedures the final energy calibration is applied to correct eventual shifts produced by neutron damage correction algorithm. This step usually is achieved using a ^{152}Eu source, counting on 13 different characteristic gamma-ray energies inside the range 122 - 1408 keV. However, a ^{60}Co calibration run was used for a statistical reason and for being closer in time to the effective acquisition runs. This, unfortunately, will results in a non optimal behavior at low energies. Fig. 4.4 shows the final energy calibration applied on crystal XXX on the ^{60}Co spectrum.
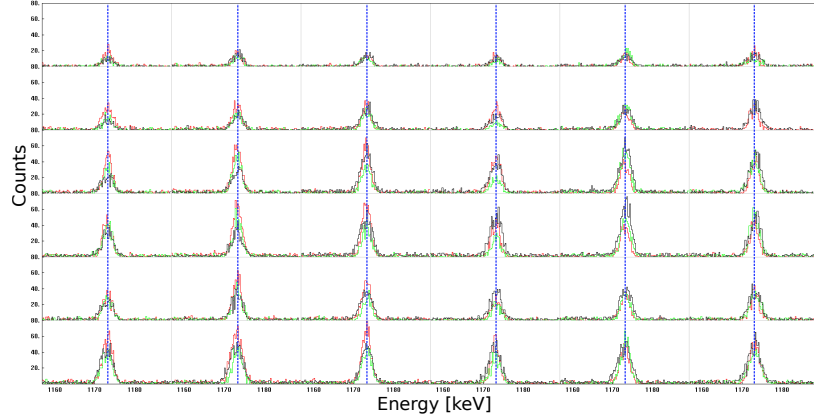

Figure 4.4: ^{60}Co 1173.2 keV peak obtained from crystals A B C of cluster 14 after final recalibration.

Finally, the last operation is a global time alignment of the cores. The time shifts to be applied to each crystal is computed minimizing the time difference between interactions belonging to the same gamma-ray event reconstructed by the tracking algorithm.

The processes described above were executed for each crystal of the array.

30

4.1.2 MUGAST

Differently from AGATA, the calibration is not applied to MUGAST data during online acquisition, which stores only the raw information and send it to NARVAL system. The event reconstruction, i.e. the coincidence between n-side and p-side signals to identify interaction position and the energy calibration, is performed offline by the analysis framework NPTool described in the following section.

A correct energy calibration of the silicon detector array is mandatory for the experiment. Together with position of interaction of light ejectiles in laboratory frame, energy of the particles are essential to reconstruct the reaction kinematic. If measured energies present differences with respect to real values a wrong excitation energy will be calculated, resulting in a systematic error in the selection of events for the angular distribution computation, as presented in the following sections. Moreover, the energy match between n-side and p-side signals is used to reject random noise events.

Each silicon strip need its own calibration parameters, with a total of $2 \times 128 \times 2 \times 10$ (parameters number)$\times$(channels number)$\times$(DSSD sides)$\times$(detectors number). This was obtained using a ^{239}Pu-^{241}Am-^{244}Cm triple alpha source with characteristic energies of 5.16-5.49-5.80 MeV respectively.

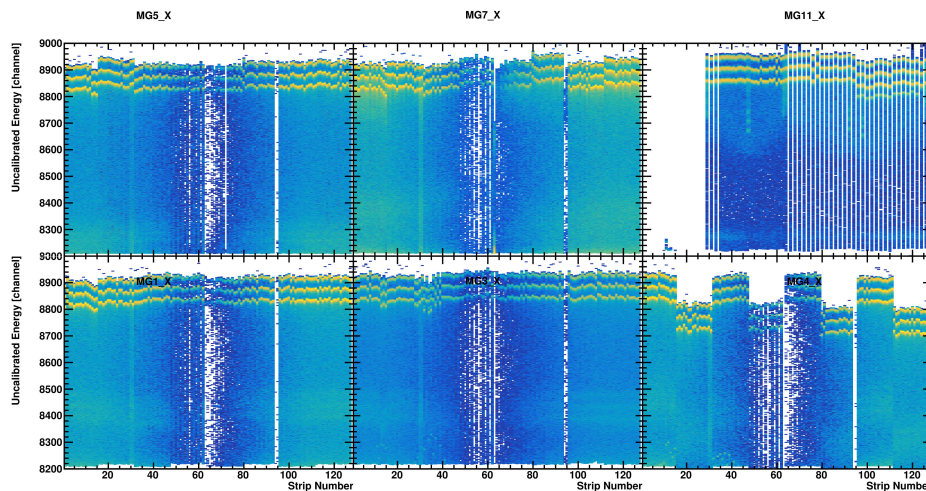The spectra used to calibrate the detectors are shown in Fig. 4.5-4.6-4.7 as reference.

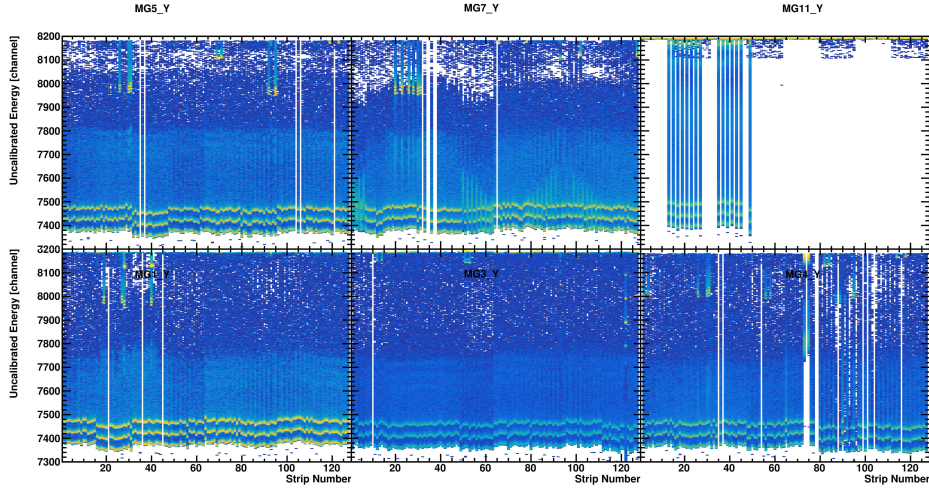Figure 4.5: Trapezoidal and Annular detectors n-side triple alpha source spectra.

Figure 4.6: Trapezoidal and Annular detectors p-side triple alpha source spectra.
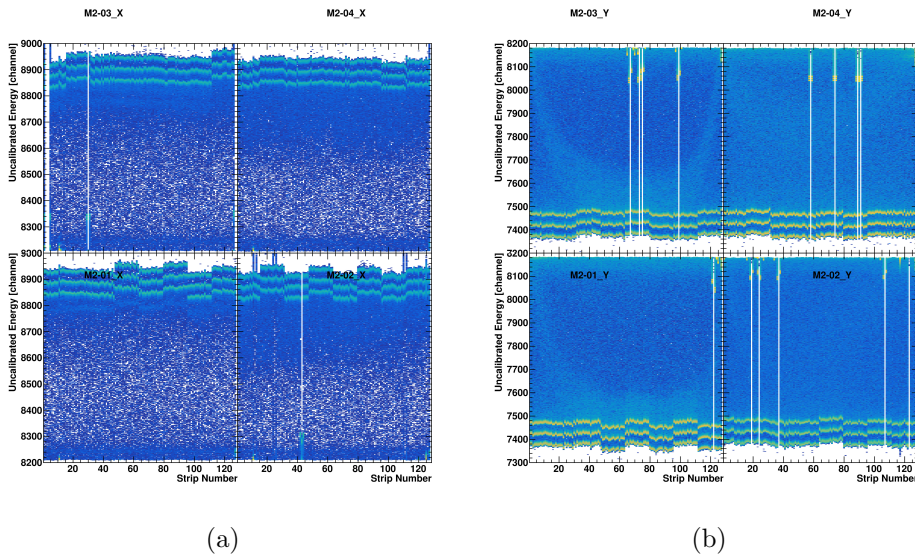

Figure 4.7: MUST2 detectors n-side (a) and p-side (b) triple alpha source spectra.

4.2 NPTool Analysis

As above mentioned, data saved on disk by NARVAL chain are ready to be analyzed or replayed using the FEMUL emulator, nevertheless MU-GAST array events are still in a raw format, i.e. having uncalibrated

energy and timing of single strips. At this stage data need to be processed by NPTool (Nuclear Physics Tool) [22] framework to extract the desired information. NPTool is an open source data analysis and Monte Carlo simulation framework specifically developed for low energy nuclear physics experiments. At the moment of this work it provides support for more than 50 different detectors setup and has been used for analysis and simulation purposes of experiments at facilities including GANIL, RIKEN, ALTO and TRIUMF. The main feature of the software is that data obtained from experiments and generated by Monte Carlo simulations are treated exactly in the same way. This behavior ensures the absence of systematic bias when comparing the two information. Fig. 4.8 shows the dependencies structure of the code. The simulation of a specific setup is carried out using NPSimulation dynamic library based on Geant4 [23] which produces an experimental like dataset. Regardless of the simulated or experimental origin of the dataset, it is then processed by npanalysis. Two different step take place at this stage: firstly, raw data are shaped using NPLib dynamic library. In the case of interest single events are reconstructed using the coincidence between n-side and p-side signals to identify interaction position while energies are calibrated. The position of interaction is converted in laboratory reference system using the survey measurements of the array. The second step is the extraction of the physical meaning quantities. This is achieved with the use of libNPAnalysis, a dynamic library generated from the compilation of Analysis macro, the real user interface part of the code. Information like excitation energy and center of mass spherical coordinates are computed and stored in the final Root TTree.
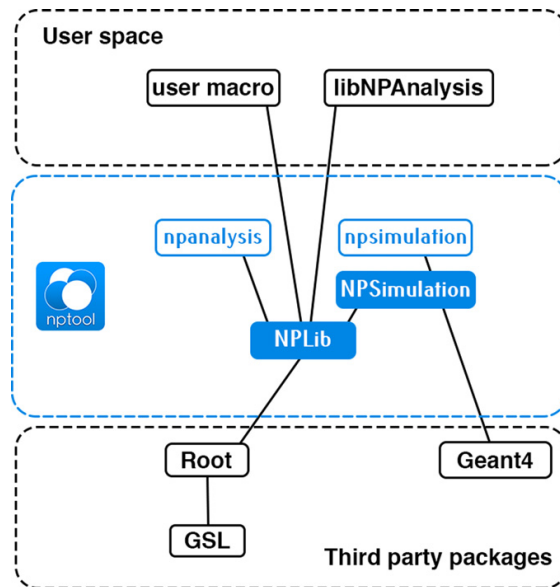

Figure 4.8: NPTool dependencies structure.

4.2.1 Efficiency Simulation

A simulation of MUGAST experimental setup was carried out. The purpose is the computation of angular efficiency of the system, necessary to renormalize experimental data for the comparison with theoretical expectations.
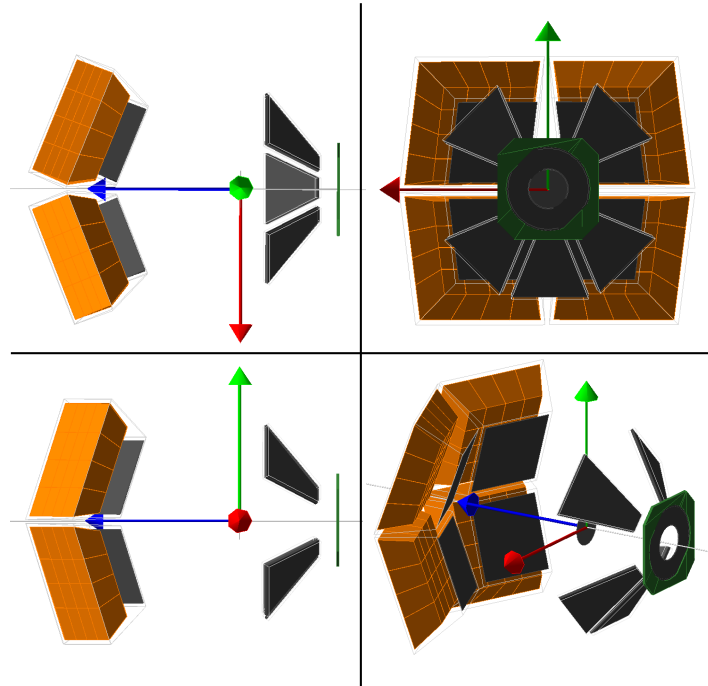

Figure 4.9: Perspective views of the setup from the three reference axis obtained from Geant4 MUGAST array simulation performed with NPTool framework.

The simulation needs as input the detector setup configuration, a reaction file containing all the information about the transfer analyzed, such as beam energy and excitation energies of the outgoing nucleus, and finally the center of mass cross section of the process analyzed. In order to retrieve the efficiency the latter was assumed to be a flat distribution, obtaining therefore a detected angular distribution (see Eq.2.3)in the center of mass frame product of the beam intensity (number of generated events), the differential cross section (constant value), target thickness and finally detection efficiency:

$$r_{\text{reaction}}\left(\theta,\phi\right) = 4\pi I_{\text{beam}} \frac{d\sigma}{d\Omega}\left[n_x \Delta x\right]\varepsilon\left(\theta,\phi\right) \tag{4.1}$$

In the analysis described in the following section only the θ angular dependence of efficiency was required, while the absolute value was accounted as

a normalization factor. Fig. 4.10 shows the normalized efficiency obtained in the center of mass frame of the reaction.
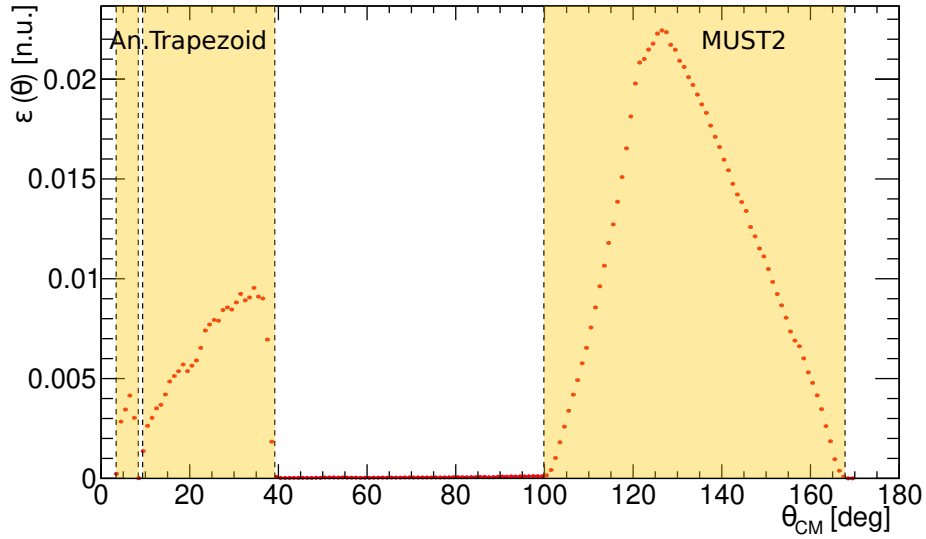

Figure 4.10: Angular efficiency of MUGAST array in center of mass reference frame of the reaction. The three highlighted bands represent the angular coverage of the annular, trapezoids and MUST2 detectors.

4.3 Angular Distribution

In order to compute the angular distribution of $l = 0$ and $l = 2$ neutron transfer reactions two statistical runs were considered (see Tab. 4.1).

	Run 256	Run 257
Start Time	2019-04-05 22:56:31	2019-04-06 09:52:28
Stop Time	2019-04-06 09:44:30	2019-04-06 16:54:03
Target	CD2 1 mg/cm^2	CD2 1 mg/cm^2
Beam intensity	~ 40 kHz	~ 40 kHz
Beam energy	6 MeV/u	6 MeV/u

Table 4.1: Main acquisition runs specification.

The CD2 target was irradiated for $\sim$11 h. with a total of $\sim 1.6 \cdot 10^9$ ^{16}O nuclei. Fig. 4.11 presents the two cumulative impact matrices of the two runs at forward and backward angles.
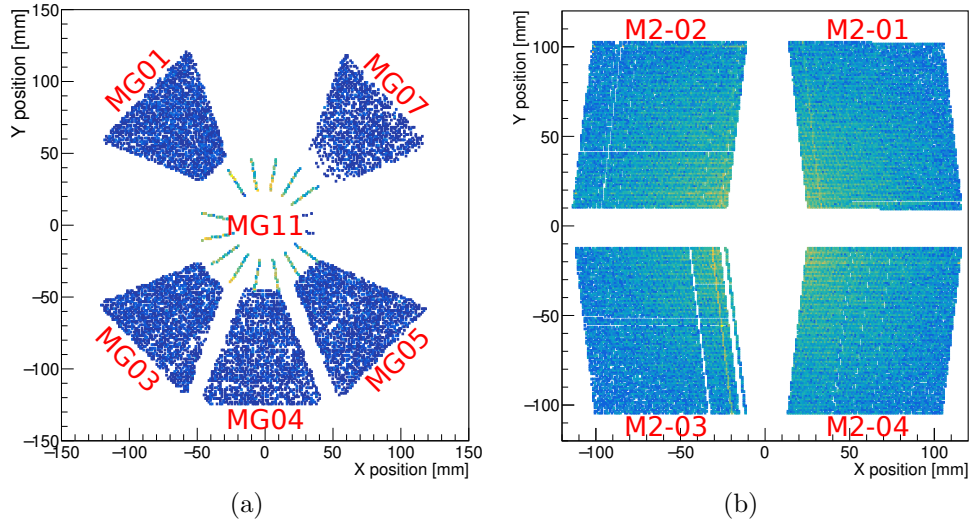
Figure 4.11: Impact matrices for trapezoids and annular detectors (a) and MUST2 telescopes (b).

Within the Analysis macro, the correction applied to reconstruct kinematic information of the reaction are on an event basis. The entrance beam energy is computed from the provided one removing the energy loss due to CD2 - ^{16}O interaction, assuming the reaction takes place at middle target. Considering an half thickness of 0.5 mg/cm^2 and an initial energy of 6 Mev/u the loss is accounted in $\sim$2 MeV. The values are computed using energy loss tables provided by Geant4 simulations. The same procedure is repeated for detected outgoing protons, using the laboratory emission angle to compute the effective path length inside the target.

Exploiting the identification capabilities of MUST2, protons at forward angles were selected using E-ΔE matrix of Fig. 4.12.
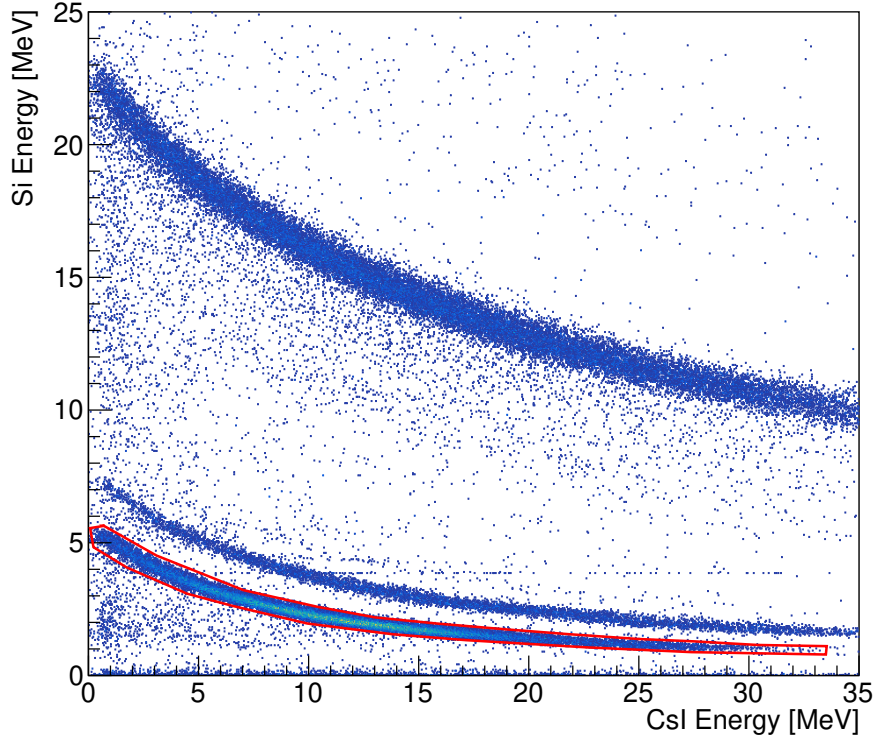
Figure 4.12: E-ΔE identification matrix on MUST2 detected events. The red selected cluster are the proton events.

With the detected particles at backward angles and gated protons on MUST2 the kinematic plot of Fig. 4.13-(a) was produced. The high protons background at forward angles on MUST2 telescope is expected to be the result of fusion evaporation reactions between ^{16}O and target ^{12}C nuclei. PACE calculations show an integrated cross section for proton evaporation over MUST2 solid angle acceptance of ∼290 mb, while expected value for the transfer reaction is ∼13 mb (forward angles have a lower transfer cross section compared to backward ones).

Accounting the impossibility to disentangle transfer and evaporated protons without other observables, the analysis was limited on trapezoids and annular detected events. Nevertheless the backward angular region is optimal for the comparison between differential cross sections for the two different momentum transfer, reaching their maximum values. Fig. 4.13-(b) present the kinematic plot at backward angles, where the two kinematic lines are clearly visible. The three decreasing line between 5-6 MeV denote the presence of an alpha calibration source contamination in the reaction chamber. The angular dependence of their energy value is due to the target energy loss correction, which is related to the particle direction and is applied to each events. This contamination does not constitute a problem, since it does not cross the kinematic lines of interest.
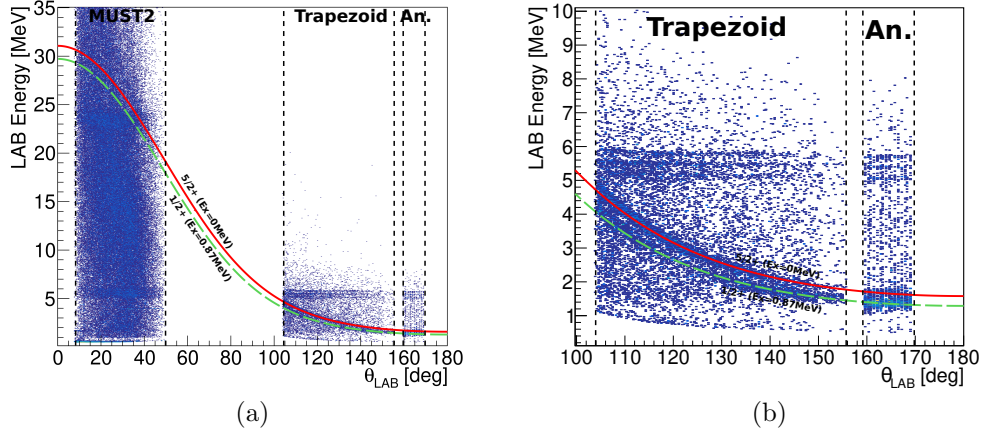
Figure 4.13: Kinematic plots obtained from the detected light particles and the gated proton events on MUST2. The different detectors angular acceptances are highlighted by dashed lines. Red and dashed green curves represent the calculated kinematic lines for $l = 2$ and $l = 0$ neutron transfer respectively.

From measured energy (E_{Lab}) and angle (θ_{Lab}) of the light particle the excitation energy of ^{17}O was computed. Naming (1)-(2) the beam and target nuclei and (3)-(4) the beam-like and target-like ejectiles, the relativistic four-momentum of proton was calculated:

$$p_3^\mu = \left(\frac{E_r}{c}, \mathbf{p}_3 \right) \tag{4.2}$$

The relativistic energy E_r and momentum vector $\mathbf{p}_3$ are given by:

$$E_r = E_{Lab} + m_3 c^2 \tag{4.3}$$
$$\mathbf{p}_3 = (p_3 \sin(\theta_{Lab}), 0, p_3 \cos(\theta_{Lab})) \tag{4.4}$$

Exploiting the four-momentum conservation p_4^μ was computed:

$$p_4^\mu = p_3^\mu - (p_1^\mu + p_2^\mu) \tag{4.5}$$

Finally, from the mass-shell condition:

$$p_4^\mu p_{4\,\mu} = m_4^{*\,2} c^2 \tag{4.6}$$

$$E_x = m_4^* c^2 - m_4 c^2 \tag{4.7}$$

The excitation energy distribution is presented in Fig. 4.14, showing clearly the presence of the two $1/2^+$ (870.73 keV) and $5/2^+$ (g.s.) levels of ^{17}O.
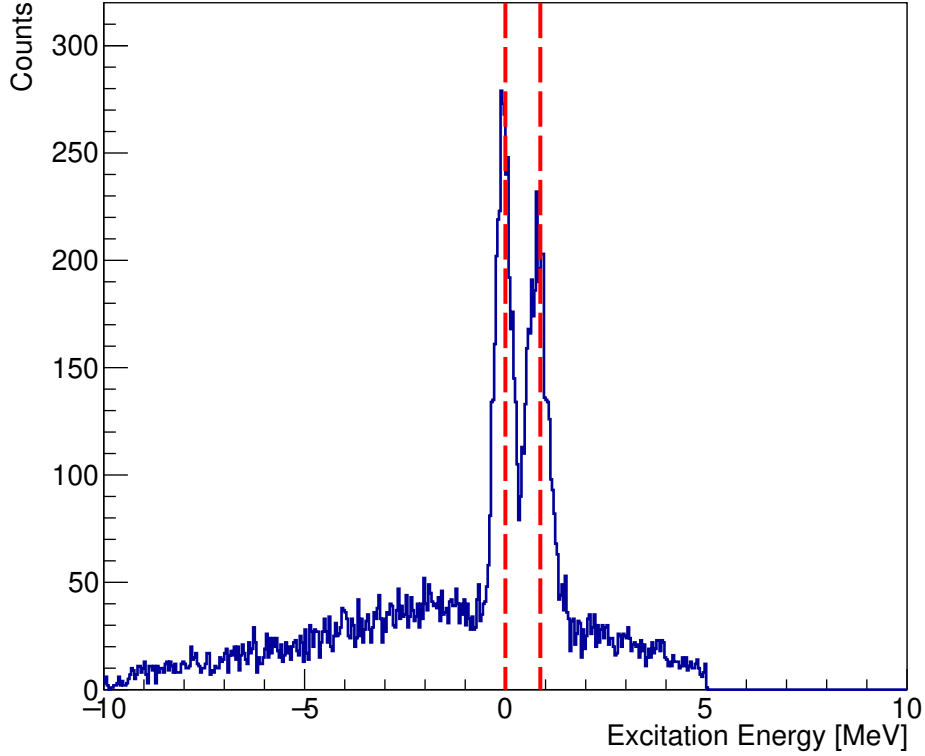
Figure 4.14: Excitation energy distribution of residual ^{17}O nuclei for backward detected protons.

Fig. 4.14 highlight a discrepancy between the measured excitation energies and the nominal ones from NNDC database [24], since the experimental values are smaller than the adopted ones. This difference can have several explanations, related to the parameters used in the excitation energy computation. Among them, target thickness, used to evaluate the energy loss of ejectiles, can be different from datasheet value and can change during the experiment. In the attempt to account this discrepancy a grid search was performed on the data measuring the excitation energies of the two level for different values of thickness. The two energies were measured with a gaussian fit of the two peaks. Fig. 4.15 shows the result of this optimization, with the measured excitations both converging to the adopted values for a thickness correction of -4.3 μm from the nominal one (1 mg/cm^2, 12.52 μm). A value so high is expected to carry inside other compensation not accounted in the analysis, being unlikely an error of $\sim$1/3 in target thickness.
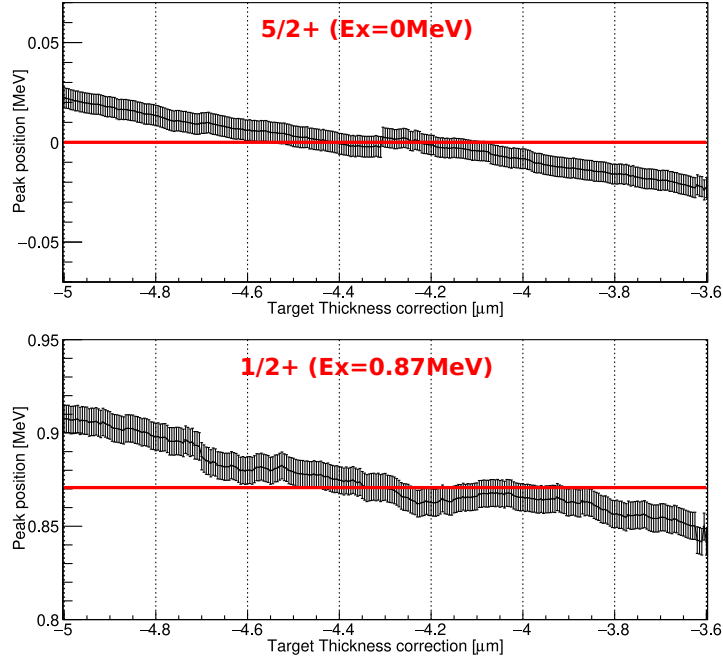
Figure 4.15: Grid search performed adding a correction to the nominal target thickness.

Using the corrected target thickness, two energy gates were applied selecting events inside FWHM area of the two peaks. Thus, angular distributions of the two transitions were measured (see Fig. 4.16).
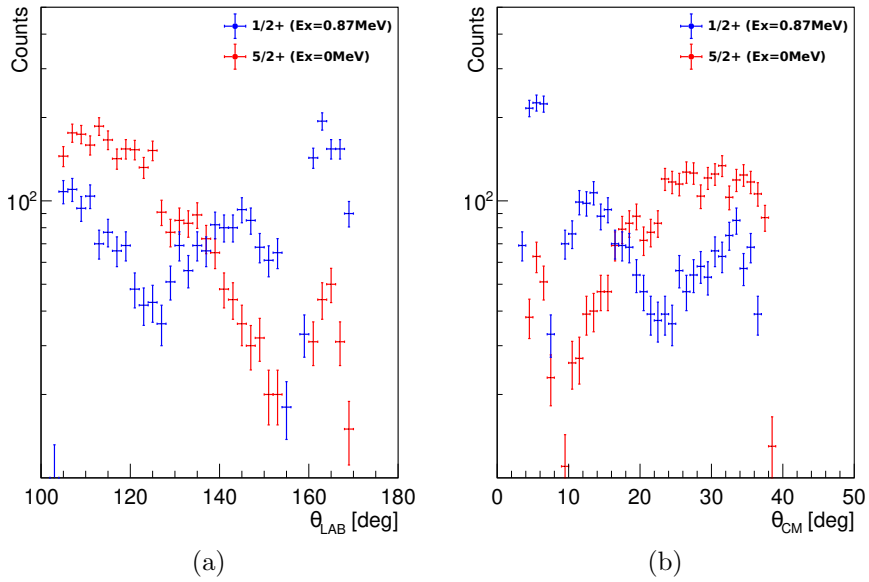

Figure 4.16: Angular distribution obtained gating events inside FWHM area of the two excitation peaks of Fig. 4.14.

In order to compare angular distributions to theoretical differential cross sections the plot of Fig. 4.16-(b) need to be corrected. The number of detected particles in the range $[\theta, \theta + \Delta\theta]$ ($\Delta\theta$ is the discretization adopted) is expressed as follow (integrating Eq.4.1):

$$\mathrm{Y}(\theta) = \mathrm{const} \times \int_0^{2\pi} \int_\theta^{\theta+\Delta\theta} \frac{d\sigma}{d\Omega}(\theta)\varepsilon(\theta)\sin(\theta)d\theta d\phi \qquad (4.8)$$

Inside the discretization range, $\frac{d\sigma}{d\Omega}(\theta)$ and $\varepsilon(\theta)$ are assumed constants and can be moved outside the integral:

$$\mathrm{Y}(\theta) = \mathrm{const} \times \frac{d\sigma}{d\Omega}(\theta)\ \varepsilon(\theta)\ \mathrm{F}(\theta) \qquad (4.9)$$

$$\mathrm{F}(\theta) = 2\pi\left(\cos(\theta) - \cos(\theta + \Delta\theta)\right) \qquad (4.10)$$
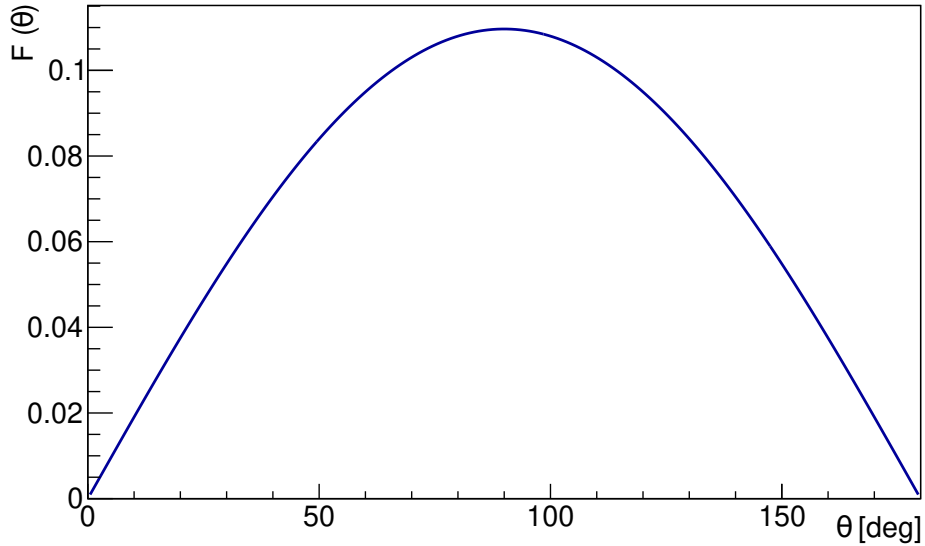

Figure 4.17: F(θ) curve as a function of θ.

Finally, renormalizing the angular distributions of Fig. 4.16 with $\varepsilon(\theta)$ and F(θ) of Fig. 4.10-4.17, a fitting of the two theoretical differential cross sections was perfomed. The fit parameter is the constant of Eq. 4.9 which accounts for beam intensity and target thickness. The final result is presented in Fig. 4.18, where the fitted distributions are compared to the theoretical ones. Inside the angular coverage of the trapezoidal detector there is an optimal agreement between the two, the same cannot be reported for the annular section where a clear difference is present. A clear explanation of this behavior has not been found at the moment of this work, further studies will be nedeed.
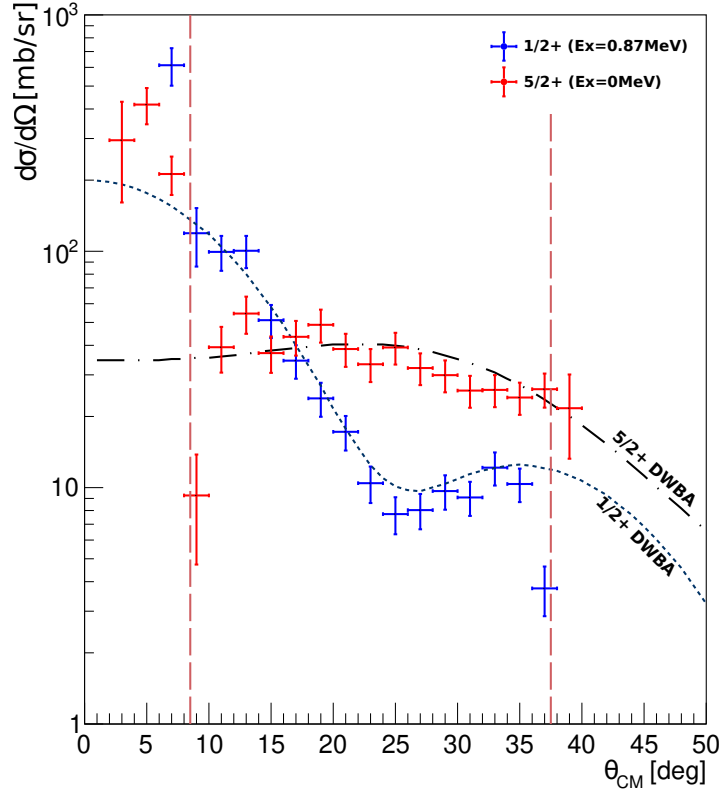
Figure 4.18: Experimental distribution fitted to theoretical differential cross sections for l=0 and l=2 transfers. The angular region limited by dashed lines is the trapezoids angular coverage.

4.4 AGATA Efficiency

The coincident detection of a proton with kinematic compatible with the excitation of the $1/2^+$ excited state of ^{17}O and the consequent emitted gamma ray allows to estimate the efficiency of the HPGe array. During the ~11 h. acquisition a total of $\sim 6.9 \cdot 10^7$ gamma rays were detected by the spectrometer. The acquired spectrum and impact matrix are reported in Fig. 4.19. The expected gamma-ray peak at 870.71 keV is completely covered by experimental background, therefore a cleaning of the spectrum is needed. In this direction a time window of 300 ns was used in the Event Merger actor to avoid uncorrelated events, and the coincidence with a proton belonging to the FWHM area of the $1/2^+$ excitation peak of Fig. 4.14 was requested. The total number of detected gamma rays with these conditions reduced to $1.1 \cdot 10^3$, producing Fig. 4.20-(a) spectrum. The peak is clearly visible, nevertheless a shift from the expected value is observed. The reason is the Doppler effect due to the velocity of ^{17}O, therefore a correction is needed.

Firstly, the four-momentum of the gamma ray emitted was computed:

$$p_\gamma^\mu = \left(\frac{E_\gamma}{c}, \frac{E_\gamma}{c}\hat{\gamma} \right) \tag{4.11}$$

$\hat{\gamma}$ is the gamma ray direction unit vector in the laboratory reference system obtained from the position of first interaction in the spectrometer. Exploiting the kinematic of protons, the four-momentum of ^{17}O was extracted from Eq. 4.5, then the velocity was computed:

$$\overline{\beta} = \frac{\mathbf{p}c}{E} = \frac{\mathbf{p}}{p^0} \tag{4.12}$$

A relativistic boost is finally applied to obtain p_γ^μ in center of mass frame, from which the original energy of the gamma ray is measured (see Fig. 4.20-(b)).

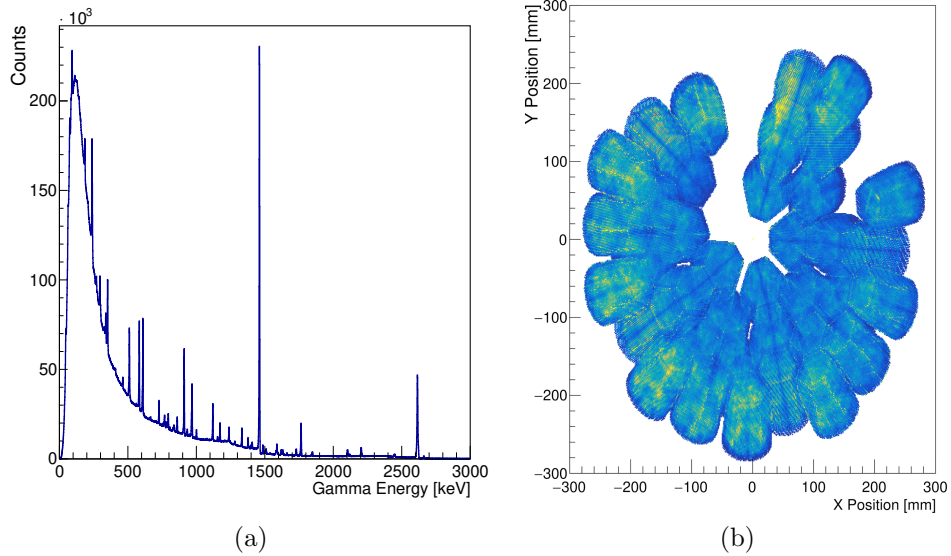(a)   (b)

Figure 4.19: Gamma-ray spectrum recorded during the experiment (a) and corresponding impact matrix of the array (b).
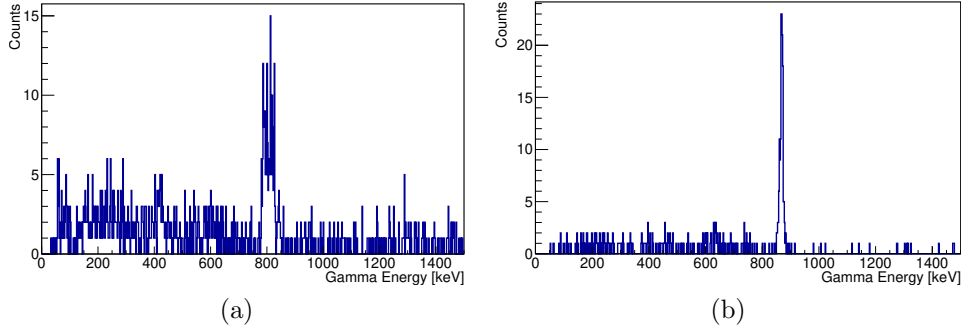
Figure 4.20: Gamma-ray raw (a) and Doppler corrected (b) spectra obtained in coincidence with a proton belonging to FWHM area of $1/2^+$ excitation peak in Fig. 4.14

The final gamma-ray peak after Doppler correction presents a little asymmetry with respect to the nominal adopted energy of 870.71 keV (see Fig. 4.21). A possible explanation of this tail can be the in-flight decay of ^{17}O outside the target, due to the 179.2 ps lifetime of the $1/2^+$ level. Moreover, the resolution obtained from the peak is worst than expected, because the reconstruction of ^{17}O kinematic from proton direction and energy has not the same quality of the VAMOS measured one, leading to a broadening in the Doppler correction.
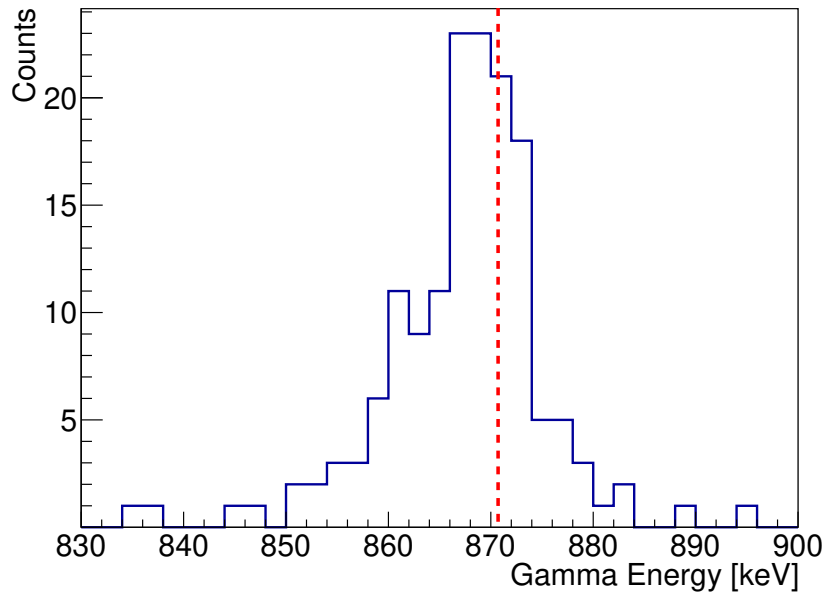

Figure 4.21: Zoom on gamma-ray doppler corrected spectrum of Fig. 4.14-(b). The dashed red line represent the adopted energy of 870.71 keV.

The efficiency was estimated counting the number of gated protons, after a background subtraction of $1/2^+$ excitation peak in Fig. 4.14, and the corresponding gamma ray in the peak of Fig. 4.20-(b), obtaining an overall value of $7.2 \pm 0.6\%$ with the tracking algorithm and $7.4 \pm 0.6\%$ with Add-back. The values are compatible with the simulated efficiency of the spectrometer, nevertheless an optimization of the Tracking parameters should be carried out, having used the the default values (minprobsig 0.15 and minprobtrack 0.05).

Proton number	γ with tracking algorithm	γ with Add-back
2035 ± 45	147 ± 12	150 ± 12

Table 4.2: Proton and gamma-ray numbers of Fig. 4.14 $1/2^+$ excitation peak and Fig. 4.20-(b).

5 Conclusion and Further Perspectives

Within this work the commissioning experiment of a new setup specifically designed for direct reaction studies was reported.

Three independent detection systems were coupled for the first time at GANIL, requiring an experimental validation of the full apparatus. In this sense a known transfer reaction was used as benchmark test to check every aspect of the setup, in order to be ready for the subsequent experimental campaign.

The goal of this experiment was the coincident detection of recoiling nuclei with VAMOS magnetic spectrometer and MUGAST Silicon array, together with the de-excitation gamma ray emitted from the heavy nuclei. Although the presence of some issues in the tuning phase of the spectrometer and the electronic readout of the square DSSD of MUGAST, later solved, the commissioning was considered a success, having obtained the required performances during the online analysis before the first scheduled experiment. The acquired data were then analyzed during the following months in order to look further in the setup capabilities.

The differential cross section of the reaction considered were reproduced and fitted to theoretical estimation obtaining an optimal agreement.

Furthermore, the coincident detection of the proton ejectile, kinematically compatible with the transfer to the $1/2^+$ excited state of ^{17}O, and the consequent gamma-ray emission allowed the computation of AGATA efficiency, obtaining a value of $\sim 7.3\%$, in good agreement with the performed simulations of the setup.

The data coming from VAMOS magnetic spectrometer were not analyzed so far, therefore further work is needed in this sense. The VAMOS kinematic information on the heavy nucleus can gain the Doppler correction resolution giving more precise results. A detailed analysis on the spectrometer efficiency during the acquisition runs is however required.

This experimental setup is an important step for the AGATA and GRIT communities towards the final development of the two full arrays, which will grant a unique window over the study of exotic nuclei.

Bibliography

[1] M. D. Cooper, W. Hornyak, and P. Roos, "Deuteron stripping to the single particle states of 17o," *Nuclear Physics A*, vol. 218, no. 2, pp. 249–273, 1974.

[2] S. Darden, S. Sen, H. Hiddleston, J. Aymar, and W. Yoh, "Study of (d, p) reactions to unbound states of 13c and 17o," *Nuclear Physics A*, vol. 208, no. 1, pp. 77–92, 1973.

[3] T. Al Kalanee, J. Gibelin, P. Roussel-Chomaz, N. Keeley, D. Beaumel, Y. Blumenfeld, B. Fernandez-Dominguez, C. Force, L. Gaudefroy, A. Gillibert, *et al.*, "Structure of unbound neutron-rich 9 he studied using single-neutron transfer," *Physical Review C*, vol. 88, no. 3, p. 034301, 2013.

[4] T. Ma, B. Guo, Z. Li, Y. Li, D. Pang, Y. Han, Y. Shen, J. Su, J. Liu, Q. Fan, *et al.*, "Precision measurement of the angular distribution for the 16o (d, p) 17o transfer reaction to the ground state of 17o," *Nuclear Physics A*, vol. 986, pp. 26–33, 2019.

[5] A. M. Moro, "Models for nuclear reactions with weakly bound systems," tech. rep., 2018.

[6] N. Glendenning, *Direct nuclear reactions*. Elsevier, 2012.

[7] H. An and C. Cai, "Global deuteron optical model potential for the energy range up to 183 mev," *Physical Review C*, vol. 73, no. 5, p. 054605, 2006.

[8] B. Watson, P. Singh, and R. Segel, "Optical-model analysis of nucleon scattering from 1 p-shell nuclei between 10 and 50 mev," *Physical Review*, vol. 182, no. 4, p. 977, 1969.

[9] C. A. Ur, "Perspectives for the gamma-ray spectroscopy at lnl: the galileo project," in *Journal of Physics: Conference Series*, vol. 366, p. 012044, IOP Publishing, 2012.

[10] S. Akkoyun, A. Algora, B. Alikhani, F. Ameil, G. De Angelis, L. Arnold, A. Astier, A. Ataç, Y. Aubert, C. Aufranc, *et al.*, "Agata—advanced gamma tracking array," *Nuclear Instruments and Methods in Physics Research Section A: Accelerators, Spectrometers, Detectors and Associated Equipment*, vol. 668, pp. 26–58, 2012.

[11] G. F. Knoll, *Radiation detection and measurement.* John Wiley & Sons, 2010.

[12] B. Birkenbach, *Gamma ray tracking with the AGATA demonstrator. A novel approach for in-beam spectroscopy.* PhD thesis, Universität zu Köln, 2014.

[13] D. Bazzacco, A. collaboration, *et al.*, "The advanced gamma ray tracking array agata," *Nuclear Physics A*, vol. 746, pp. 248–254, 2004.

[14] A. Lopez-Martens, K. Hauschild, A. Korichi, J. Roccaz, and J. Thibaud, "γ-ray tracking algorithms: a comparison," *Nuclear Instruments and Methods in Physics Research Section A: Accelerators, Spectrometers, Detectors and Associated Equipment*, vol. 533, no. 3, pp. 454–466, 2004.

[15] S. Colosimo *et al.*, *The characterisation of AGATA high purity germanium detectors for pulse shape analysis.* PhD thesis, University of Liverpool, 2013.

[16] Y. Blumenfeld, F. Auger, J. Sauvestre, F. Maréchal, S. Ottini, N. Alamanos, A. Barbier, D. Beaumel, B. Bonnereau, D. Charlet, *et al.*, "Must: A silicon strip detector array for radioactive beam experiments," *Nuclear Instruments and Methods in Physics Research Section A: Accelerators, Spectrometers, Detectors and Associated Equipment*, vol. 421, no. 3, pp. 471–491, 1999.

[17] E. Pollacco, D. Beaumel, P. Roussel-Chomaz, E. Atkin, P. Baron, J. Baronick, E. Becheva, Y. Blumenfeld, A. Boujrad, A. Drouart, *et al.*, "Must2: A new generation array for direct reaction studies," in *The 4th International Conference on Exotic Nuclei and Atomic Masses*, pp. 287–288, Springer, 2005.

[18] M. Rejmund, B. Lecornu, A. Navin, C. Schmitt, S. Damoy, O. Delaune, J. Enguerrand, G. Fremont, P. Gangnant, L. Gaudefroy, *et al.*, "Performance of the improved larger acceptance spectrometer: Vamos++," *Nuclear Instruments and Methods in Physics Research Section A: Accelerators, Spectrometers, Detectors and Associated Equipment*, vol. 646, no. 1, pp. 184–191, 2011.

50

[19] M. Siciliano, *Nuclear structure of the semi-magic tin isotopes close to 100Sn: lifetime measurements of low-lying states in 106Sn and 108Sn.* PhD thesis, Università di Padova, Dipartimento di Fisica e Astronomia" G. Galilei", 2017.

[20] X. Grave, R. Canedo, J.-F. Clavelin, S. Du, and E. Legay, "Narval a modular distributed data acquisition system with ada 95 and rtai," in *14th IEEE-NPSS Real Time Conference, 2005.*, pp. 5–pp, IEEE, 2005.

[21] B. Bruyneel, B. Birkenbach, J. Eberth, H. Hess, G. Pascovici, P. Reiter, A. Wiens, D. Bazzacco, E. Farnea, C. Michelagnoli, *et al.*, "Correction for hole trapping in agata detectors using pulse shape analysis," *The European Physical Journal A*, vol. 49, no. 5, p. 61, 2013.

[22] A. Matta, P. Morfouace, N. De Séréville, F. Flavigny, M. Labiche, and R. Shearman, "Nptool: a simulation and analysis framework for low-energy nuclear physics experiments," *Journal of Physics G: Nuclear and Particle Physics*, vol. 43, no. 4, p. 045113, 2016.

[23] S. Agostinelli, J. Allison, K. a. Amako, J. Apostolakis, H. Araujo, P. Arce, M. Asai, D. Axen, S. Banerjee, G. . Barrand, *et al.*, "Geant4—a simulation toolkit," *Nuclear instruments and methods in physics research section A: Accelerators, Spectrometers, Detectors and Associated Equipment*, vol. 506, no. 3, pp. 250–303, 2003.

[24] D. Tilley, H. Weller, and C. Cheves, "Energy levels of light nuclei a= 16–17," *Nuclear Physics A*, vol. 564, no. 1, pp. 1–183, 1993.